AGU PUBLICATIONS

JGR

Journal of Geophysical Research: Oceans

RESEARCH ARTICLE

10.1002/2013JC009331

Companion to *Yao et al.* [2014] doi:10.1002/2013JC009004.

Key Points:

- Sinking occurs in a narrow boundary layer along the eastern boundary
- Surface western boundary current switches into an eastern boundary current
- Water exchange in the Strait of Bab el Mandeb is not hydraulically controlled

Correspondence to:
I. Hoteit,
ibrahim.hoteit@kaust.edu.sa

Citation:
Yao, F., I. Hoteit, L. J. Pratt, A. S. Bower, A. Köhl, G. Gopalakrishnan, and D. Rivas (2014), Seasonal overturning circulation in the Red Sea: 2. Winter circulation, *J. Geophys. Res. Oceans*, *119*, 2263–2289, doi:10.1002/2013JC009331.

Received 6 AUG 2013
Accepted 26 JAN 2014
Accepted article online 20 MAR 2014
Published online 14 APR 2014

Seasonal overturning circulation in the Red Sea: 2. Winter circulation

Fengchao Yao[1], Ibrahim Hoteit[1], Larry J. Pratt[2], Amy S. Bower[2], Armin Köhl[3], Ganesh Gopalakrishnan[4], and David Rivas[5]

[1]Division of Physical Sciences and Engineering, King Abdullah University of Science and Technology, Thuwal, Saudi Arabia, [2]Department of Physical Oceanography, Woods Hole Oceanographic Institution, Woods Hole, Massachusetts, USA, [3]Institut für Meereskunde, Zentrum für Meeres- und Klimaforschung, Universität Hamburg, Hamburg, Germany, [4]Scripps Institution of Oceanography, San Diego, La Jolla, California, USA, [5]CICESE, Oceanografia Biologica, Ensenada, Baja California, Mexico

Abstract The shallow winter overturning circulation in the Red Sea is studied using a 50 year high-resolution MITgcm (MIT general circulation model) simulation with realistic atmospheric forcing. The overturning circulation for a typical year, represented by 1980, and the climatological mean are analyzed using model output to delineate the three-dimensional structure and to investigate the underlying dynamical mechanisms. The horizontal model circulation in the winter of 1980 is dominated by energetic eddies. The climatological model mean results suggest that the surface inflow intensifies in a western boundary current in the southern Red Sea that switches to an eastern boundary current north of 24°N. The overturning is accomplished through a cyclonic recirculation and a cross-basin overturning circulation in the northern Red Sea, with major sinking occurring along a narrow band of width about 20 km along the eastern boundary and weaker upwelling along the western boundary. The northward pressure gradient force, strong vertical mixing, and horizontal mixing near the boundary are the essential dynamical components in the model's winter overturning circulation. The simulated water exchange is not hydraulically controlled in the Strait of Bab el Mandeb; instead, the exchange is limited by bottom and lateral boundary friction and, to a lesser extent, by interfacial friction due to the vertical viscosity at the interface between the inflow and the outflow.

1. Introduction

The overturning circulation in the Red Sea exhibits a distinct seasonal variation with reversed regimes. In the first part of this two-part study [*Yao et al.*, 2014], we showed that a 50 year high-resolution MIT general circulation model (MITgcm) simulation with realistic atmospheric forcing and bottom topography could successfully reproduce the seasonal cycle of the exchange structure in the Strait of Bab el Mandeb (hereafter referred to as the strait) and the summer subsurface intrusion of the Gulf of Aden intermediate water. The simulation showed that the summer overturning circulation in the Red Sea is controlled by both remote winds in the north Indian Ocean through the shoaling of the thermocline in the Gulf of Aden and the local surface wind stress over the Red Sea, which sets up a surface slope enhancing the subsurface pressure gradient and intrusion.

The winter overturning circulation has been the subject of more theoretical and modeling studies than the summer overturning circulation because the annual mean circulation in the Red Sea is dominated by the winter regime and is characterized by the production and export of high-salinity Red Sea outflow water [*Phillips*, 1966; *Eshel and Naik*, 1997; *Sofianos and Johns*, 2002, 2003]. Waters below the 100–200 m deep pycnocline in the Red Sea exhibit distinct properties with almost uniform temperature and salinity and are conventionally called the Red Sea deep waters, although this term creates some ambiguity. Three different sources were proposed by *Wyrtki* [1974] for the formation of the Red Sea deep water: two overflows from the Gulf of Aqaba and Gulf of Suez and deep convection in the northern Red Sea. Analysis of the distributions of geochemical tracers, such as ^{14}C and ^{3}He [*Cember* 1988], and dissolved oxygen concentrations [*Woelk and Quadfasel*, 1996; *Sofianos and Johns*, 2007] indicated that the Red Sea deep waters are composed of two distinct water masses. In the upper part of the deep waters above 300 m or so, water characterized by its high concentration of dissolved oxygen is formed mainly in the northern Red Sea at

intermediate depths below the pycnocline [*Cember* 1988], which drives a shallow overturning circulation in the Red Sea. The distributions of the geochemical tracers and the dissolved oxygen concentration also suggest a deep overturning circulation driven by overflows from the Gulf of Suez formed intermittently during anomalously cold winters [*Woelk and Quadfasel*, 1996]. However, observations of chlorofluorocarbons [*Plahn et al*., 2002] suggested that the densest water mass in the northern Red Sea comes from the Gulf of Aqaba. With a formation rate of 0.11 $\pm$ 0.02 Sv as estimated by *Cember* [1988], the shallow overturning circulation associated with water mass formation at the intermediate depths is stronger than the deep overturning circulation, which has an estimated formation rate of 0.05 $\pm$ 0.01 Sv. The modeling study by *Sofianos and Johns* [2003] supported this observation and suggested that the Red Sea outflow water in the strait is supplied by the intermediate water formed in the northern Red Sea. In this part of the study, we focus on the shallow winter overturning circulation. The deep overturning circulation will be investigated in future studies.

Because of its elongated shape, the Red Sea is often treated two dimensionally in theoretical studies. *Phillips* [1966] considered a two-dimensional, turbulent convective model for the winter overturning circulation in the Red Sea and presented similarity solutions that are able to produce the basic overturning structure when vertical profiles of viscosity and diffusivity are given [*Tragou and Garret*, 1997]. However, the modeling studies by *Eshel and Naik* [1997], *Sofianos and Johns* [2003], and *Biton et al*. [2008] suggested that the circulation in the Red Sea has a more complex three-dimensional structure. Their studies suggested that energetic mesoscale eddies and gyres are present, with current speeds one order of magnitude higher than the speed of the vertical overturning circulation. Furthermore, they found intensified boundary currents along both the eastern and western boundaries, although they each showed significantly different spatial structures of the Red Sea circulation.

These three-dimensional studies did not offer conclusive evidence on the structure and location of the sinking and the formation of the deep water in the winter overturning circulation in the Red Sea. *Sofianos and Johns* [2003] suggested that the deep water is formed in a cyclonic gyre in the northern Red Sea that is exported through a large-scale baroclinic adjustment. *Eshel and Naik* [1997] suggested that the sinking occurs close to the western boundary due to a collision of the returning eastern boundary current with the northward western boundary current. Recent modeling and experimental studies on thermally forced marginal seas [*Spall and Pickart*, 2001; *Spall*, 2003, 2004; *Pratt and Spall*, 2008; *Pedlosky and Spall*, 2005; *Cenedese*, 2012] suggested that, for a basin subject to buoyancy loss like the Red Sea, the actual sinking takes place in a narrow region near the boundaries. In this setting, vorticity that is generated by stretching associated with the downward motion is balanced by frictional diffusion due to the boundary.

Clearly, basic questions regarding the three-dimensional structure of the overturning circulation and the location and dynamics of the sinking process during the winter overturning in the Red Sea remain unanswered. Here we present in section 2 the results on the three-dimensional structure of the winter surface inflow, the sinking location and the intermediate outflow, according to the model. We then diagnose and interpret the dynamical mechanisms that drive the overturning circulation in the context of previous theoretical studies in section 3. We analyze the dynamics and hydraulics in the strait in section 4. Finally, we present a summary of the winter overturning circulation and dynamics in section 5.

2. Model Results

The model domain consists of the Red Sea, the Gulf of Aqaba, the Gulf of Suez, and part of the Gulf of Aden, with an eastern boundary located at the Gulf of Aden (Figure 1). The horizontal grids are defined on curvilinear coordinates rotated along the axis of the Red Sea, and the along-basin and cross-basin velocities in the following text are referring to, respectively, as the velocities in the direction along the axis and across the axis of basin in the rotated domain. A nearly 50 year simulation from January 1952 to December 2001 is run, forced with 6 h NCEP reanalysis atmospheric data. The detailed configurations of the simulation are described in *Yao et al.* [2014]. The seasonal variability of the overturning circulation in the Red Sea dominates the variability in the 50 years of the simulation, with relatively weak interannual variability, as indicated in the water exchange in the strait [Figure 3, *Yao et al*., 2014]. As in the study of the summer overturning circulation in *Yao et al.* [2014], much of the analysis here focuses on a single year, namely 1980. As shown in the next subsection, 1980 is a typical year in that it closely follows the mean seasonal

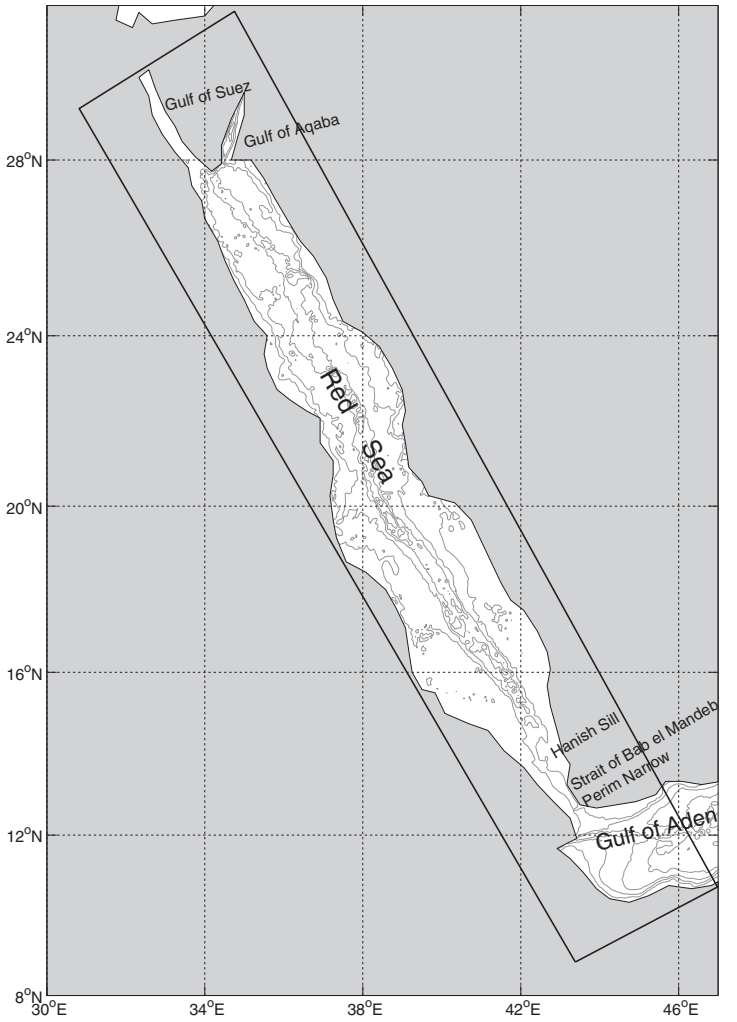

Figure 1. Bathymetry of the Red Sea and the MITgcm model domain. Contour intervals are 500 m starting from 100 m. The model domain is indicated by the black box.

variability. At the same time, because the currents associated with the overturning circulation, being one order weaker in magnitude, are obscured by the much stronger mesoscale eddies except in the strait (e.g., Figure 5), the monthly mean fields averaged over 50 years of the simulation are used to extract the spatial structure of the sinking process in the northern Red Sea.

2.1. Surface Fluxes and Seasonal Thermal Responses in the Northern Red Sea

The surface fluxes, including the net fresh water flux (net evaporation rate), heat flux, and surface wind stress are calculated from bulk formula from the atmospheric state variables (wind speed, air temperature, specific humidity, precipitation, and short-wave and long-wave radiation) in the NCEP reanalysis data and the model sea surface temperature. The seasonal variations of the surface fluxes are critical in forcing the water mass formation process and the overturning circulation. The annual cycles of heat flux, net fresh water flux and buoyancy flux over the Red Sea in 1980 from the model results are plotted in Figure 2a. The seasonal pattern of the surface wind stress is more relevant to the summer circulation, and it is shown in Figure 2 in *Yao et al.* [2014]. The heat flux and net evaporation rate have annual mean values of 9.1 W m^{-2} (heat loss from the sea) and 1.9 m yr^{-1}, respectively, which are in good agreement with the estimated annual mean values based on observations of the exchange flow in the strait by *Sofianos et al.* [2002]. In contrast to the modeling study of *Sofianos and Johns* [2002], no correction is applied to the heat flux and evaporation rate. The heat flux exhibits a strong seasonal cycle with a large annual range of over 200 W m^{-2} and dominates the resultant annual cycle of the buoyancy flux over the Red Sea. However, the annual

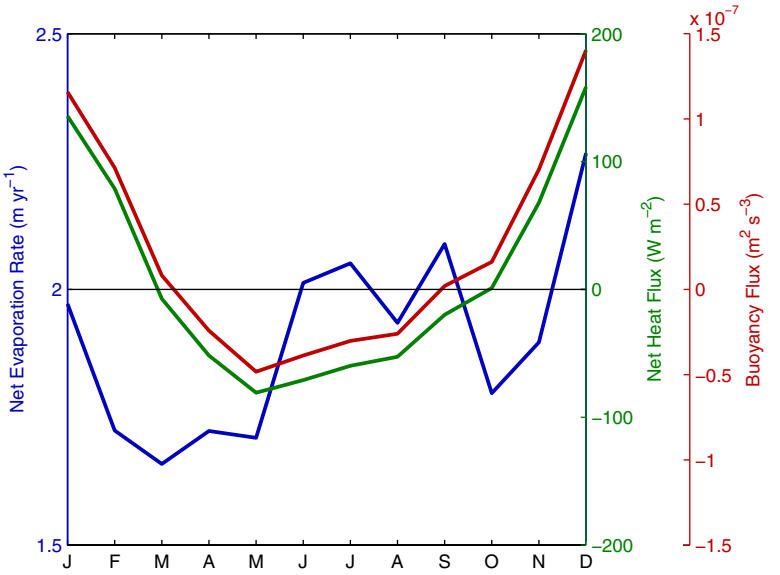

Figure 2a. Annual cycle of the net evaporation rate, net heat flux, and the resultant buoyancy flux over the surface in the Red Sea for 1980 from the model result. Positive values indicate fluxes from the sea to the air.

mean buoyancy flux, 2.0×10^{-8} m^2 s^{-3}, is largely contributed by the annual mean net evaporation over the Red Sea. For a typical spatial distribution in February, both the evaporation and heat loss in the Red Sea increase almost linearly from about 18°N to the north (Figure 2b), with the largest buoyancy loss occurring north of 24°N.

In response to the surface fluxes, the vertical temperature structure in the northern Red Sea, which is linked to water mass formation processes, exhibits distinct and repeated seasonal cycles, as illustrated by the annual cycles of vertical temperature averaged north of 24°N for 1980 and 1981 in Figure 3a. During the winter in each year, surface cooling leads to deep convection in the northern Red Sea and the mixed layer depth (calculated as the depth where the temperature is 0.2°C lower than the surface temperature) deepens to ~150 m. Waters with an almost vertically uniform temperature of about 22°C are thereby formed. In contrast, during the summer, surface warming increases the surface temperature to over 28°C and the mixed layer depth reduces to less than 30 m (Figure 3a). There is clearly interannual variability as suggested by the seasonal cycles of the surface temperature and the mixed layer depth in the 50 years of simulation (Figures 3b and 3c). The surface temperatures in the 50 years follow a repeated seasonal cycle with a range of interannual variability of about 2°C. Conversely, the mixed layer depths during winters show a large range of variability of about 100 m in different years, mainly because of the sensitivity of the calculation to the small gradient in the vertical temperature profiles. Overall, the seasonal variability of the vertical thermal structure associated with the water mass formation processes in the northern Red Sea predominates over the interannual variability in the 50 years of simulation. As shown by the thin black curve in Figures 3b and 3c, the sea surface temperature and mixed layer depth in 1980 closely follow the mean structure of the seasonal variation. By these measures, 1980 is regarded as a representative year in the following analysis.

2.2. Winter Overturning Circulation

The winter overturning circulation for the upper 400 m in the Red Sea is presented in Figure 4, which plots the monthly mean overturning stream functions integrated across the basin, along with axial salinity and temperature sections for February 1980. Reversed from the summer circulation, the overturning cell is composed of a surface inflow from the Gulf of Aden and a deep outflow through the strait. The overturning cell extends to the northern end of the basin and gradually deepens from 160 m around the strait to almost 300 m in the northern Red Sea. Most of the surface inflow sinks north of 24°N and forms the southward deep outflow that reaches a maximum transport of about 0.6 Sv at the latitudes south of 24°N in the basin. Because the overturning stream functions are obtained by integrating in level space rather than in density

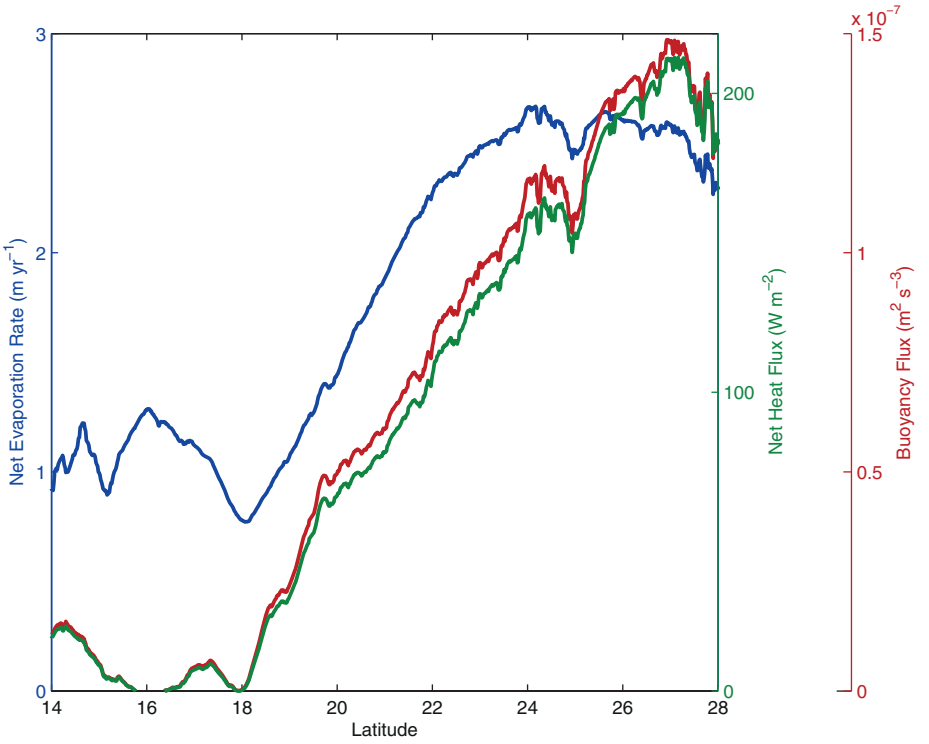

Figure 2b. The axial distribution of the net evaporation rate, net heat flux, and the resultant buoyancy flux averaged across the Red Sea for February 1980 from the model result.

space, the volume transports in the strait have slightly lower values due to the averaging across the tilting interface between the inflow and the outflow.

The winter thermohaline structures along the axis are closely related to the overturning circulation (Figures 4b and 4c). In the upper 90 m, the surface inflow undergoes a gradual salinity increase as it approaches the northern Red Sea, whereas the surface temperature reaches a maximum of about 26°C between 16 and 20°N and then a decrease to the north. From the south to the north along the axis of the Red Sea, the evaporation rate has a range of about 1 to 2.5 m yr^{-1}, while the surface heat loss has a larger range of about 0 to 200 W m^{-2} (Figure 2b). This suggests that the surface salinity distribution is an accumulative effect of the evaporation in the Red Sea, while the surface temperature in the northern Red Sea, experiencing significant seasonal variability (Figure 3), is more of a response to the local heat flux. Corresponding to the sinking locations in the overturning circulation (to be described below), deep convections take place north of 24°N as indicated by the outcropping isotherms and isohalines and the almost uniform water properties in the upper 300 m. Water with a temperature of about 22°C and salinity of about 40 psu formed in the northern Red Sea feeds the intermediate outflowing water that occupies the space between about 100 m and 300 m in the whole basin.

A cyclonic eddy centered around 25°N as suggested by the subsurface elevation of the isotherms and isohalines in the depths below 200 m is favorable for producing locally colder and saltier waters. This is consistent with the suggestion by *Sofianos and Johns* [2003] in that cyclonic eddies tend to precondition the vertical stratification and facilitate water mass transformation by trapping the water that is subject to heat and freshwater loss. However, most of the cold, salty water is formed north of 26°N and there is no clear association of the ventilation of the intermediate water with the cyclonic and anticyclonic eddies in the far north (see also Figure 5).

It is interesting to note that smaller scale, enclosed cells are embedded in the large-scale overturning cell in the northern Red Sea. They appear to be related to the location of eddies, if compared closely with the locations of the depressions and elevations of the subsurface isotherms and isohalines. A locally enhanced overturning cell tends to occur where there is an anticyclonic eddy, for instance, the cell located around 26°N.

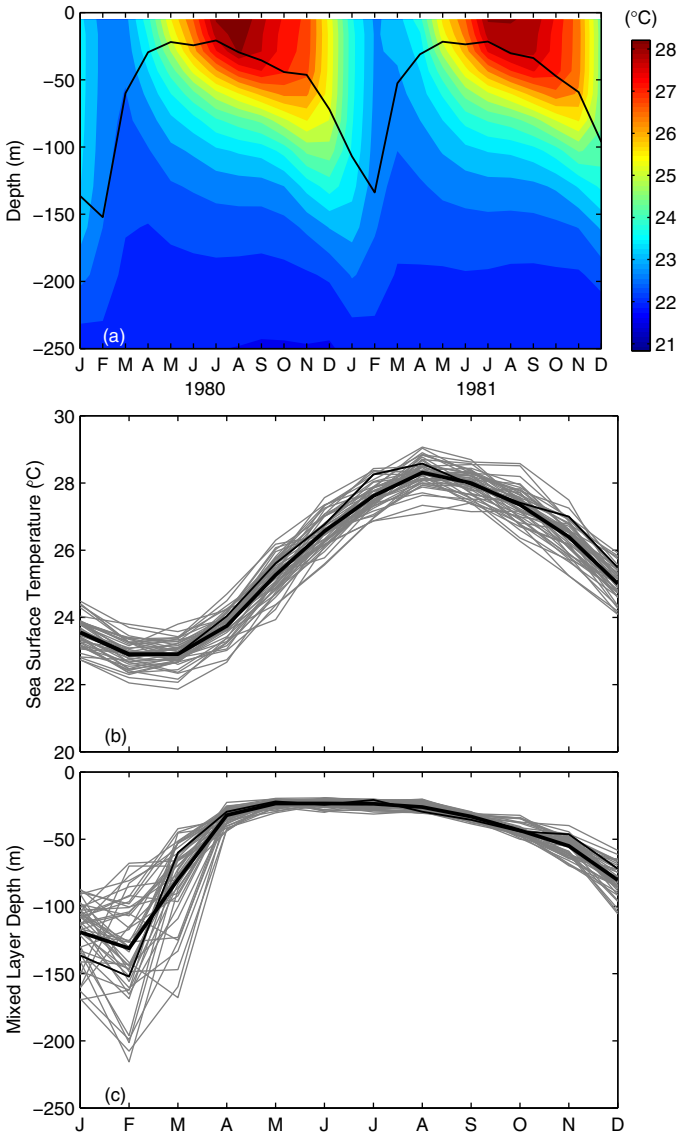

Figure 3. Seasonal response of the northern Red Sea to the surface heat flux: (a) seasonal cycles of vertical temperature averaged north of 24°N for 1980 and 1981, and seasonal cycles of sea surface temperatures (b) and mixed layer depths (c) averaged north of 24°N for each of the 50 years of simulation. The black line in Figure 3a indicates the mixed layer depth. The thick and thin black lines in Figures 3b and 3c indicate the 1980 values and the mean values, respectively.

There is no such enclosed cell in the overturning stream functions in the climatological mean (not shown here), which share a very similar pattern except for these cells. The dynamical mechanism of the short-term effect of eddies on the overturning circulation is not clear.

2.3. Surface Circulation

In comparison to the overturning structure in the latitude-depth plane, the circulation in the Red Sea exhibits complex horizontal patterns. To investigate the full three-dimensional structure of the winter overturning circulation, the horizontal fields of the surface inflow and the intermediate outflow are presented in the following subsections along with the spatial distribution of the sinking.

The surface current and salinity fields for February 1980 are shown in Figure 5. In the southern Red Sea (excluding the region with shallow coastal bathymetry between 14 and 17°N), the current field is characterized by a pronounced western boundary current with speeds of about 0.3 m s^{-1}. Two anticyclonic eddies located at about 18°N and 20°N are attached to the boundary current and these eddies continue to exist in the summer circulation [Figure 5a, *Yao et al.*, 2014]. The surface salinity increases from about 36 psu in the strait to about 40 psu in the northern Red Sea.

North of 22°N, the boundary currents are not clearly distinguishable and the current field is characterized by alternating anticyclonic and cyclonic eddies. The eddy fields are less organized than in the summer [Figure 5a, *Yao et al.*, 2014] and are in an evolving stage. This suggests that the eddy formation processes may be more related to the winter overturning circulation.

With most of the mesoscale eddy currents removed, the climatological mean fields for February reveal more details of the spatial structure of the surface inflow associated with the overturning circulation (Figures 6a and 6b). Both western and eastern boundary currents emerge in the northern Red Sea in the climatological mean fields. The western boundary current south of 22°N (not shown) is similar to that in February 1980 in terms of strength and spatial pattern. The figures show only the region north of 22°N to focus on the details of the boundary currents in the northern Red Sea. Between 24°N and 25°N, the western boundary current from the southern Red Sea splits into a weak western boundary current and an eastward cross-basin current that turns

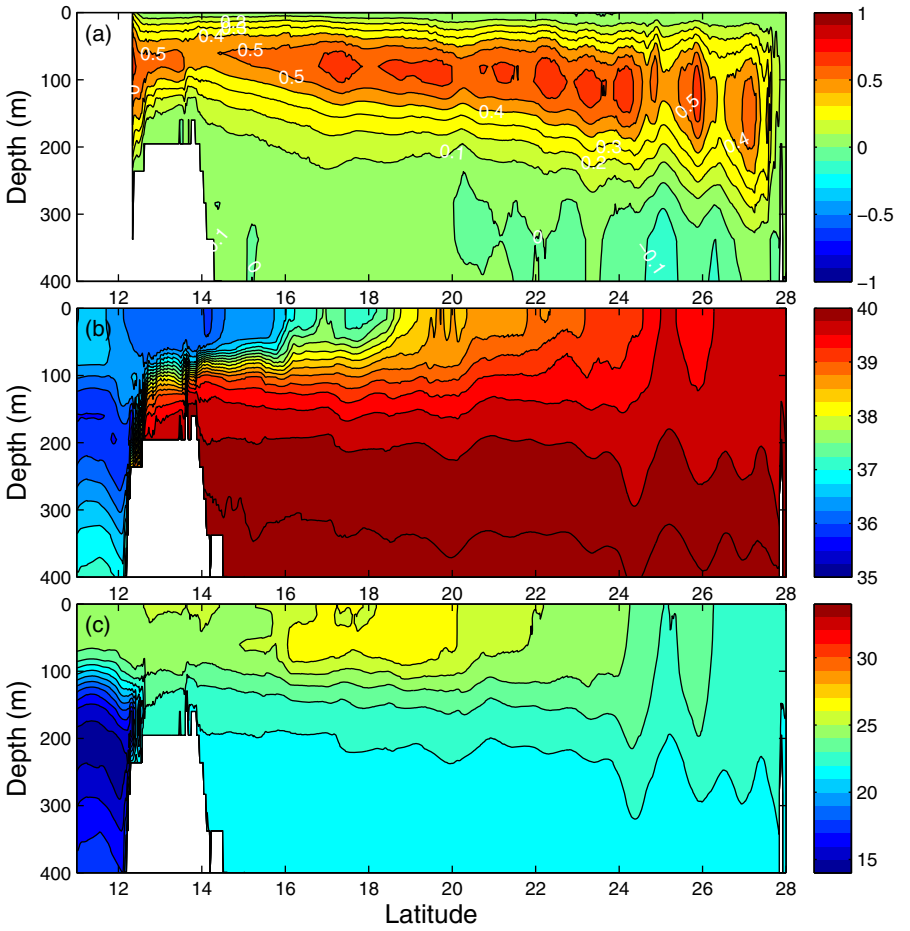

Figure 4. Monthly mean overturning circulation in the model for February 1980: (a) integrated overturning stream function (Sv), (b) axial salinity (psu) section, and (c) temperature (°C).

into an eastern boundary current along the coast. The crossing latitude of the western boundary current is farther north than in *Sofianos and Johns* [2003], in which it is located at about 16°N for the simulation with full atmospheric forcing and at about 19°N for simulation forced without surface wind stress. The eastward cross-basin currents become less pronounced north of 25°N. Similar to the climatological mean summer surface circulation [see Figure 5b, *Yao et al.*, 2014], a persistent eddy centered at about 26.8°N is present.

The eastern boundary current in the northern Red Sea brings relatively fresh and warm water to the northern end of the basin as indicated by the fresh and warm tongue along the eastern coast. It has surface velocities as large as 0.2 m s^{-1} and volume transports of about 0.40 Sv. It wraps around the northern coast of the Red Sea, where the saltiest and coldest surface water is found. For the western boundary current, which has weaker surface velocities and transports of only 0.10 Sv, the northward advection of warm waters is weaker and there is no clearly defined fresh and warm tongue. Another major feature of the surface circulation is the cyclonic recirculating gyre between 24°N and 28°N, which is formed by the eastern boundary current that turns southward around the eddy at around 26.8°N and feeds a returning, southward flow in the western part of the basin. The cold water in the northwestern corner is advected southward by this southward flow. The modeled pattern of the eastern boundary current and warm tongue in the northern Red Sea is evident in the sea surface temperature data for February averaged from the 1985–2001 Advanced Very High Resolution Radiometer (AVHRR) satellite data (Figure 7). The coldest sea surface temperature in the satellite data in the Red Sea also occurs in the northwestern corner of the basin. However, the cold surface region extends much farther to the south in the satellite data and results in a larger, cross-basin temperature gradient between 24°N and 26°N. It is possible that the model underestimates the magnitude and/or extent of the southward flowing, western portion of the cyclonic gyre. It could also be the case that the model overestimates the overall eddy diffusion and/or eddy viscosity, which would tend to

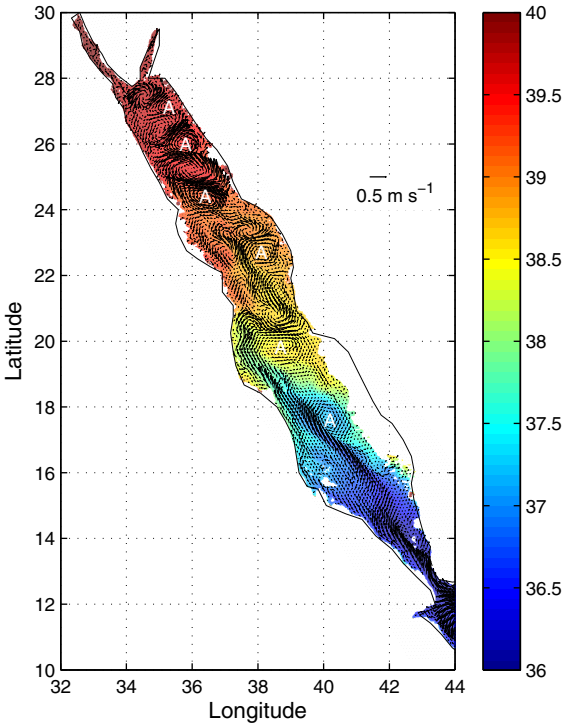

Figure 5. Surface fields of current and salinity (psu) for February 1980. Anticyclones are marked with "A"s. The blank region along the eastern coast between 16 and 18°N represents the shallow banks with complex bathymetry that are not well resolved in the model.

make boundary currents narrower and concentrate temperature anomalies closer to the boundaries as discussed later. The forcing mechanism of the boundary currents and their relation to the overturning circulation are discussed in section 3.

2.4. Sinking Processes

The spatial distribution of the sinking of the water is examined using the climatological mean fields of vertical velocity, since the fields in 1980 or other specific years show very noisy patterns. The vertical velocity for February in the climatological mean at 115 m depth in the northern Red Sea is shown in Figure 8. Downwelling is found in a narrow boundary layer about 20 km wide along the eastern boundary north of 24°N. Meanwhile, an analogous narrow boundary layer of upwelling of similar width is found along the western boundary. The boundary layer thickness is comparable to the first-mode baroclinic deformation radius, which is about 18 km in the northern Red Sea (estimated from the formula, $(g'h)^{1/2}/f$, with $g' = 0.01$ m s^{-2}, $h = 115$ m, and $f = 0.6 \times 10^{-4}$). The vertical velocities in the interior are characterized by much smaller values with irregular patterns.

The downwelling and upwelling structures adjacent to the boundaries in relation to the along-basin and cross-basin currents and the hydrographic structure are presented in a cross-basin section with its center located approximately at 25.5°N (Figure 9). The intensified vertical motions along the boundaries are present throughout the depth range over which the general overturning cell penetrates, e.g., about the upper 300 m at this section. The eastern surface boundary current extends down to about 130 m, whereas the weaker, western surface boundary current extends down to only 50 m. Consistent with the boundary upwelling and downwelling (and also with the thermal wind relation), the isotherms and isohalines bend upward in the western boundary and bend downward at the eastern boundary. The surface fields of temperature in the model (Figure 6b) and the satellite surface temperature data (Figure 7) do not give a clear signal of a cold western boundary layer associated with the upwelling. This is probably due to the southward current adjacent to the western boundary that advects the cold water in the northwestern corner and makes any cold surface temperature signal along the western boundary undetectable.

The vertical section of cross-basin velocity shows a surface eastward flow and an intermediate westward flow, both of which intensify close to the eastern boundary. Since the surface cross-basin currents in the western part of the section are very weak as shown in Figure 9, the intensified surface cross-basin currents near the eastern boundary are supplied by the cross-basin flow in the surface recirculating cyclonic gyre located between 24°N and 28°N (Figures 6a and 6b). The recirculation gyre is also manifested by the surface interior southward (negative) flow across the western half of the section (Figure 9). Even though this gyre is relatively weak compared to the persistent eddy around 26.8°N, it is crucial for facilitating the sinking along the eastern boundary as discussed later.

The presence of an eastward flow in the upper layer and a westward flow directly beneath (Figure 9) raises the question of whether the vertical volume flux close to the boundary is a result of direct sinking of the

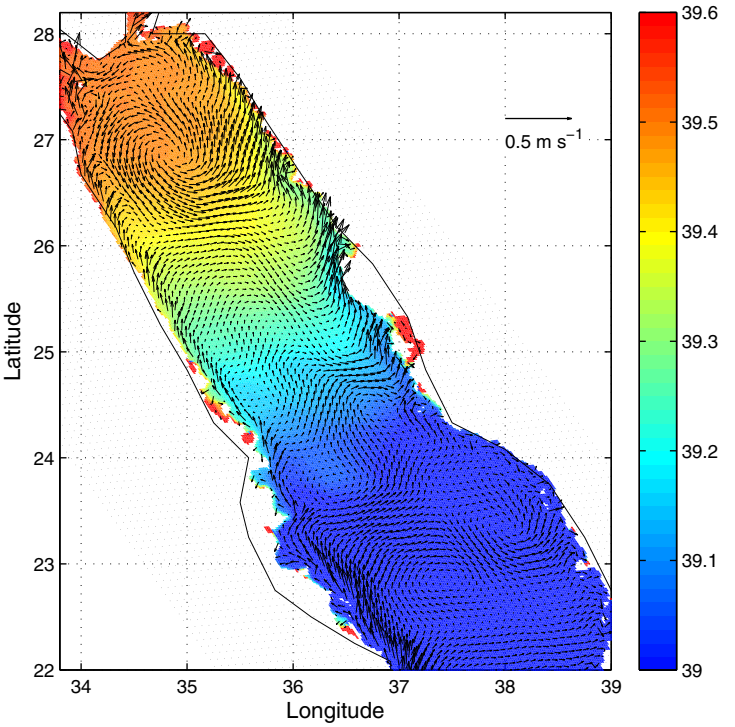

Figure 6a. Surface fields of current and salinity (psu) in February for the climatological mean. The current vectors are plotted on every fourth model grid point in both directions.

onshore flow. This is exactly what happens in an idealized study of the Atlantic overturning circulation by *Cessi and Wolf* [2009]. There, the mass balance near the eastern boundary is approximately two dimensional, with the onshore flow balanced by the sinking. To determine whether a similar balance occurs at the

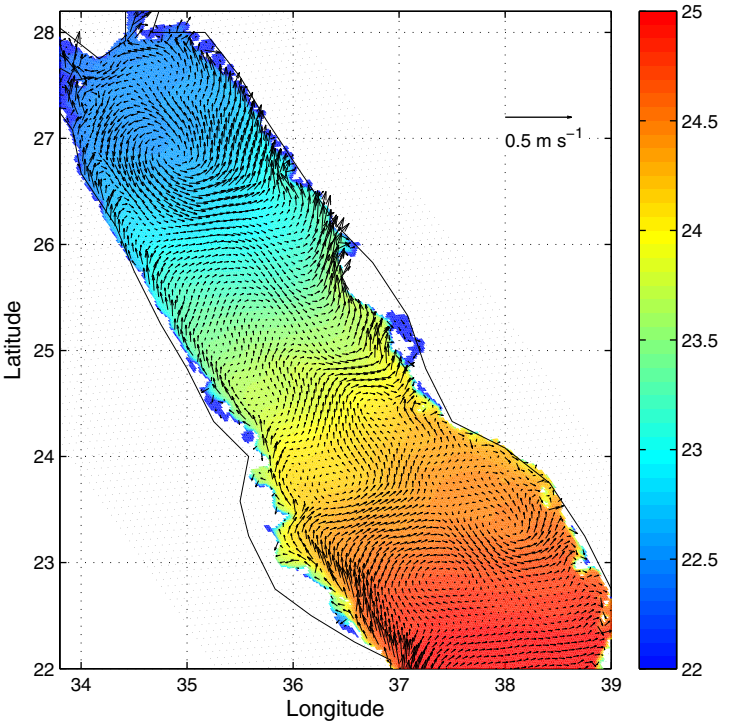

Figure 6b. Surface fields of current and temperature (°C) in February for the climatological mean.

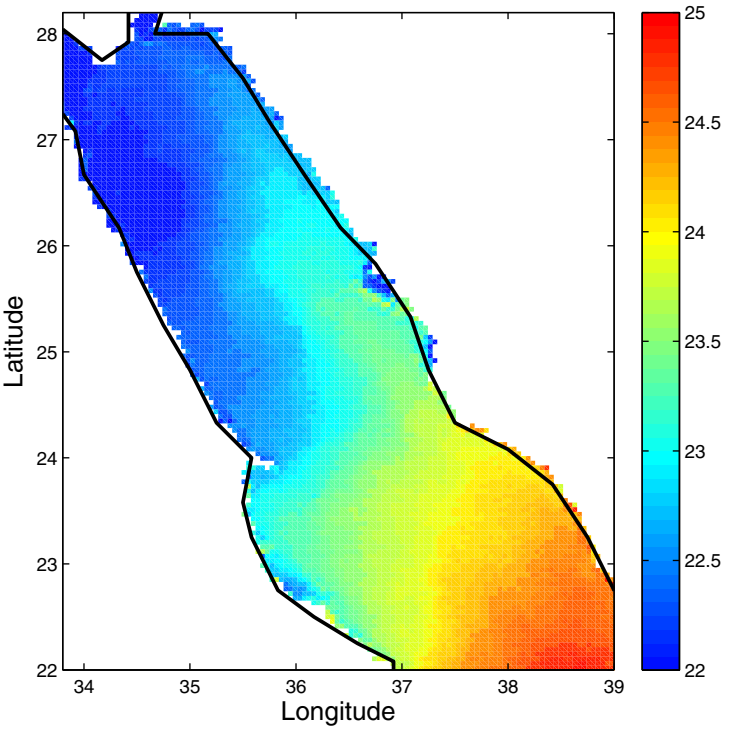

Figure 7. Sea surface temperature (°C) in the northern Red Sea for February averaged from the 1985–2001 AVHRR satellite data.

eastern boundary of the present model, we compute horizontally averaged vertical velocity over the area spanning 25°N to 28°N and extending from the coast to 20 km offshore. The resulting depth profile of the average vertical velocity is compared to the value that would result from complete sinking of the onshore

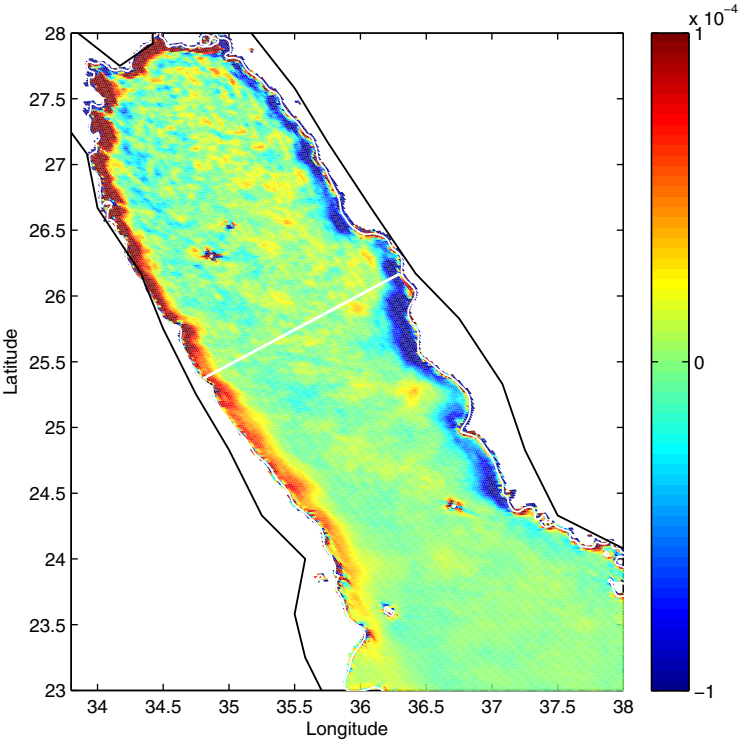

Figure 8. Vertical velocities (m s^{-1}) at the depth of 115 m in February for the climatological mean. The white line across the basin denotes the location of the section in Figure 9, and the white line along the coast denotes the 200 m isobath.

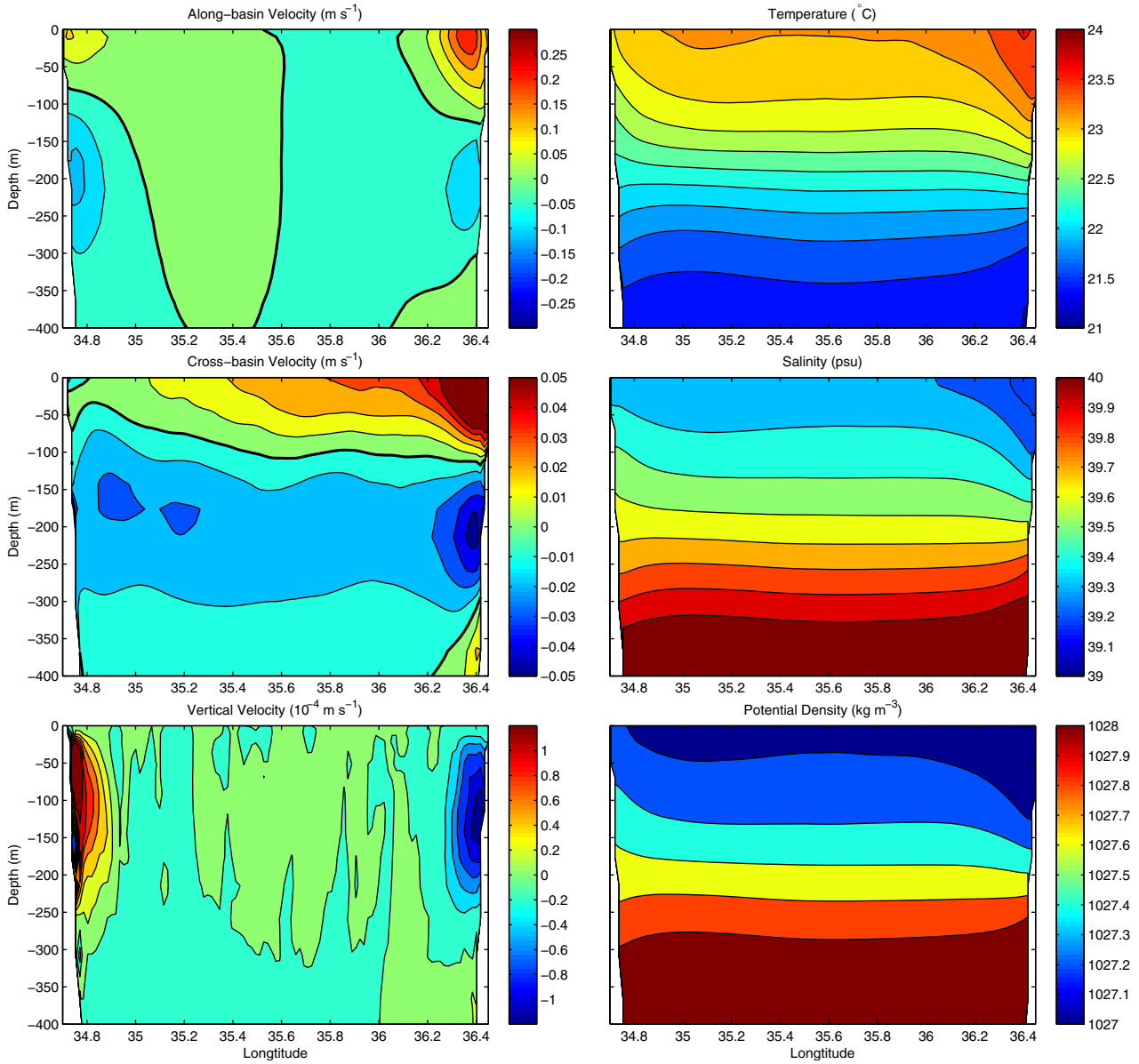

Figure 9. Vertical sections of along-basin, cross-basin and vertical velocities and temperature, salinity and potential density along the cross-basin section with center located at 25.5°N (see Figure 8 for location) in February for the climatological mean.

flow at the seaward edge of the boundary current, i.e., the derived vertical velocity by integrating the cross-basin velocity at 20 km offshore (Figure 10). The region immediately south of 25°N is not included due to its different dynamical structure; there, a jet-like cross-basin flow that crosses the Red Sea collides with the eastern boundary and turns northward, forming the strong, along-shore flow.

The averaged downwelling velocity in the eastern boundary is markedly stronger than the western upwelling velocity through the upper 300 m, and the eastward flow in the upper layer adjacent to the eastern boundary is also stronger (Figures 10a and 10b). The maximum vertical velocities at both boundaries occur at 115 m, collocated approximately with the interface between the eastward surface flow and westward intermediate flow. In the upper layer above 115 m, the derived vertical velocity profiles in both boundaries match closely with the ones in the model, indicative of mass balances between the cross-basin flows and the vertical mass fluxes in the boundary layer as in *Cessi* and *Wolf*'s [1999] model. This further suggests that a substantial portion of the onshore flow sinks along the eastern boundary and the upwelling along the

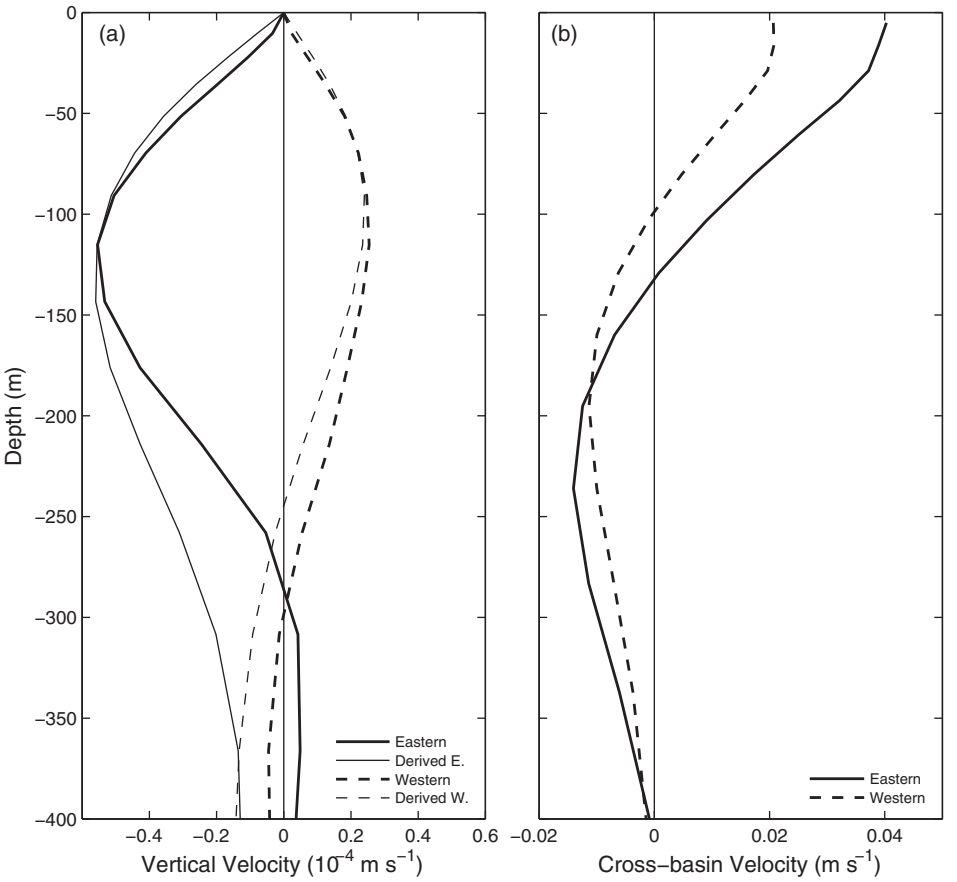

Figure 10. (a) Profiles of vertical velocity in the western and eastern boundary layers averaged between 25°N and 28°N (heavy lines) and derived vertical velocity from integration of the cross-basin velocity at the seaward edge of the boundary layers (thin lines); (b) Cross-basin velocity profiles along the seaward edges of the boundary layers averaged between 25°N and 28°N.

western boundary roughly balances the offshore flow along the western boundary. In accordance with the two-dimensional mass balance, the volume transports of the along-basin eastern and western surface boundary currents shown in Figure 9 substantially remain constant along the coasts.

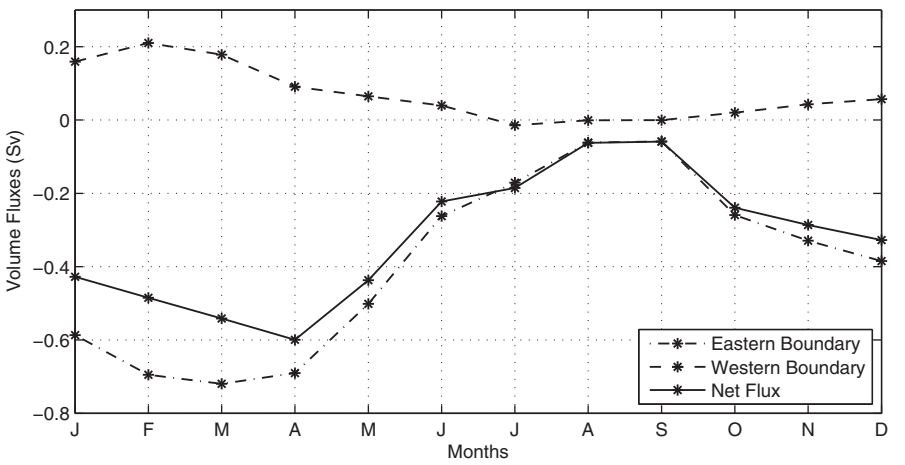

Figure 11. Vertical volume fluxes north of 24°N at the depth of 115 m in February for the climatological mean. Downwelling along the eastern boundary and upwelling along the western boundary are calculated separately.

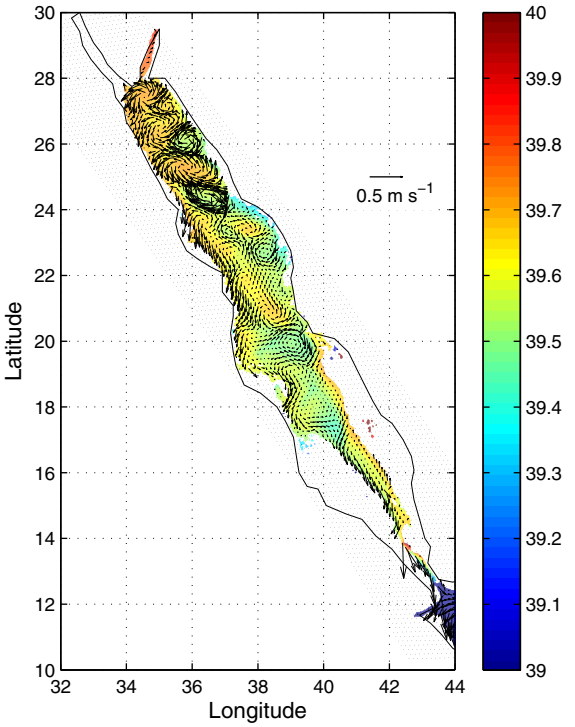

Figure 12. Fields of current and salinity (psu) at 160 m for February 1980.

In the lower layer below 115 m, the westward flows adjacent to both boundaries exhibit a similar vertical structure with maximum velocities occurring in the depths of 150–250 m. The derived vertical velocity profiles in both boundaries deviate significantly from the model ones, suggesting that the two-dimensional mass balance is not satisfied. As shown in Figures 13a and 13b in next subsection, deep boundary currents are present due to the imbalance. Along the western boundary, the westward flow in the lower layer is too strong for the upwelling to balance and part of it is diverted to contribute to a subsurface western boundary current. Similarly, the downwelling along the eastern boundary is stronger than the westward cross-basin flow and a deep eastern boundary current is formed (Figures 13a and 13b). In summary, the strength of downwelling/upwelling along the boundary is mainly determined by the cross-basin flow adjacent to the boundary.

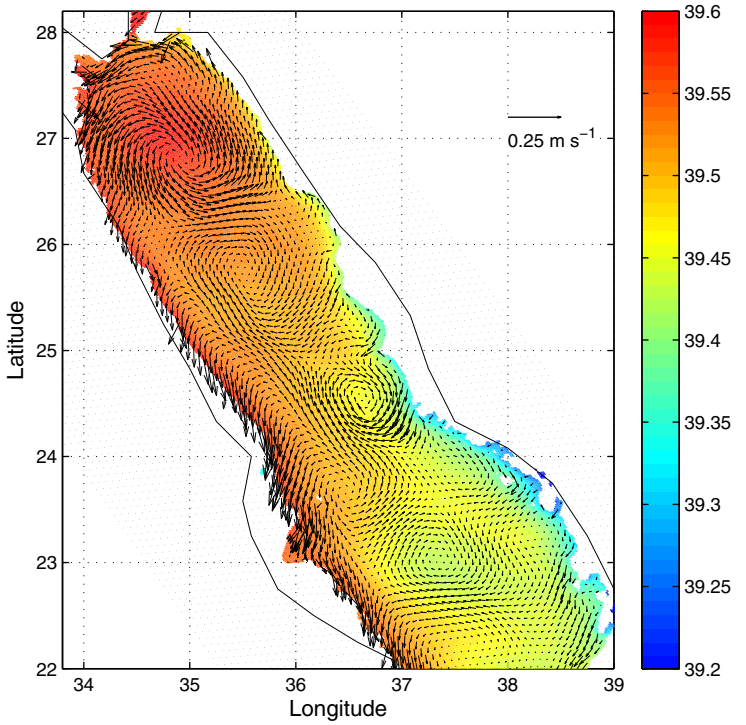

Figure 13a. Fields of current and salinity (psu) at 160 m in February for the climatological mean.

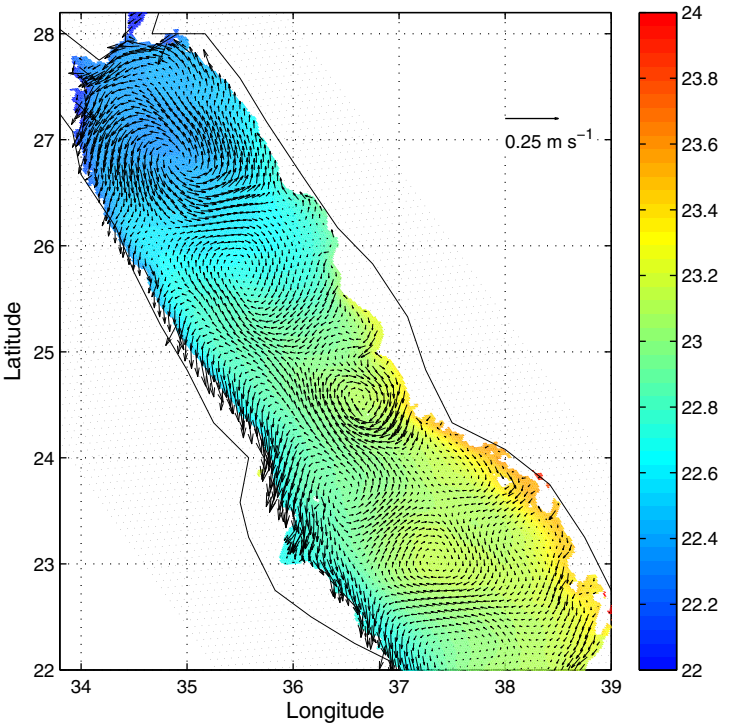

Figure 13b. Fields of current and temperature (°C) at 160 m in February for the climatological mean.

The annual cycles of the downwelling and upwelling rates across 115 m integrated north of 24°N are displayed in Figure 11. The downwelling reaches its maximum value of about 0.7 Sv in March and its minimum values about 0.05 Sv in August and September. The annual mean value for the downwelling is 0.39 Sv. The upwelling rate along the western boundary follows a similar pattern with a much smaller annual mean rate of 0.07 Sv. The net annual mean downwelling rate is 0.32 Sv, which is significantly larger than the value of 0.11 Sv in *Cember* [1988] estimated from three sparsely distributed vertical profiles of ^{14}C and ^{3}He. At the same time, the mean transport of outflow for the 50 years of simulation as presented in *Yao et al.* [2014] is

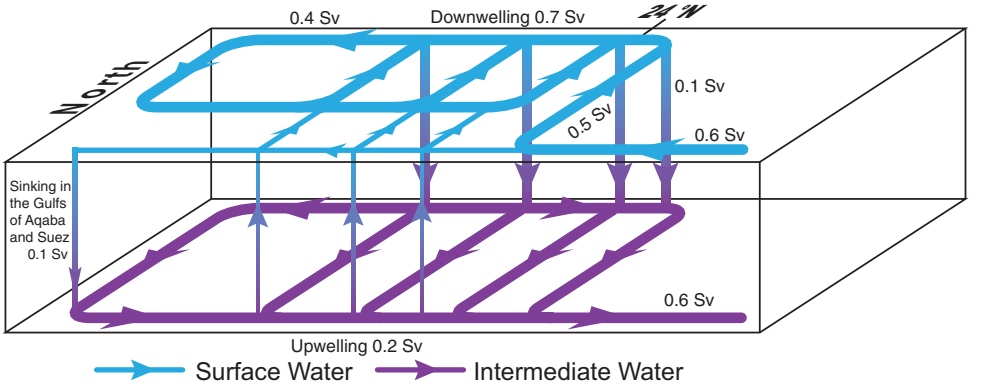

Figure 14. Schematic for the three-dimensional overturning circulation in the northern Red Sea. Most (0.5 Sv) of the surface western boundary current (0.6 Sv) crosses the basin at around 24°N, and then either sinks along the eastern boundary at the crossing latitude (0.1 Sv) or switches to an eastern boundary current (0.4 Sv) and sinks along the eastern boundary through a cyclonic recirculation. The downwelled water at the intermediate depth is transported to the western boundary either through direct cross-basin flows or a rim current along the boundary. Meanwhile, the sinking along the eastern boundary is enhanced by a weaker cross-basin overturning circulation produced by the upwelling along the western boundary (0.2 Sv). A small portion of the western boundary current (0.1 Sv) sinks in the Gulf of Aqaba and Gulf of Suez and contributes to the intermediate and deep water.

0.38 Sv and compares well with the annual mean outflow transport of 0.36 Sv estimated from direct observations in the strait by *Murray and Johns* [1997]. This suggests that most of the outflow in the strait is supplied by the downwelled waters along the eastern boundary north of 24°N and no net sinking takes place south of 24°N. The mismatch of 0.06 Sv between the downwelled water and the outflow through the strait in the model can be attributed to the dense outflows produced in the Gulf of Aqaba and the Gulf of Suez. The detailed processes of the export of these waters will be reported in a separate study.

2.5. Intermediate Circulation

To illustrate the horizontal distribution of the intermediate outflow, the current and salinity fields at 160 m for February 1980 are shown in Figure 12 and the climatological mean fields are shown in Figures 13a and 13b. Both the currents in 1980 and in the climatological mean exhibit a pronounced southward subsurface western boundary current south of 24°N. Vertically the subsurface western boundary current approximately occupies the depths between 100 and 300 m (Figure 9). Similar to the surface circulation, the intermediate circulation for February 1980 is dominated by eddies in the northern part of the Red Sea, and the formation process of the subsurface western boundary current is revealed by the climatological mean fields. Figures 13a and 13b suggest that the subsurface western boundary current is supplied by the downwelled water along the eastern boundary by two pathways: a cyclonic rim current through the northern end of the basin, which originates from the downwelling along the eastern boundary north of 26°N and outflows from the Gulfs of Aqaba and Suez, and westward cross-basin currents from the eastern boundary south of 26°N. As a result, the subsurface western boundary current experiences a downstream strengthening south of 26°N, reaching a volume transport of about 0.60 Sv at 23°N.

The three-dimensional sinking process of the winter overturning circulation in the northern Red Sea is summarized in Figure 14. Between 24 and 25°N, the surface western boundary current (0.60 Sv, the volume transport in February) splits into two branches with a small portion (0.10 Sv) propagating further north and the rest (0.50 Sv) switching to the eastern boundary after crossing the basin. The strength of the western branch remains constant along the boundary and supplies most of the deep water formation in the Gulfs of Aqaba and Suez. The eastern branch, after sinking of about 0.10 Sv around the crossing latitudes, flows northward to the northern end of the basin with a constant strength (0.40 Sv). As it turns southwestward around the northern boundary of the basin, some of it enters the Gulfs of Aqaba and Suez, and the majority joins the southward flow in the cyclonic gyre. The sinking along the eastern boundary is supplied by the eastward flow associated with the recirculation gyre and the upwelled water (0.20 Sv, Figure 11) from the western boundary. The net downwelled water (0.50 Sv) and outflows from the Gulfs of Aqaba and Suez (0.10 Sv) together form the surface western boundary current (0.60 Sv), which is exported through the strait. The strength of sinking along the eastern boundary in other winter months differs from February (Figure 11), but the overturning structure remains qualitatively unchanged.

2.6. Heat Balances in the Sinking Processes

During the sinking process, the water along the eastern boundary becomes denser due to decreasing temperature and increasing salinity. Eddy fluxes of buoyancy have been shown to be an important mechanism for the buoyancy balance near a boundary [*Spall*, 2003; *Cessi and Wolfe*, 2009]. For simplicity, we use the heat balance to investigate the roles of different processes on the buoyancy balance. The temperature, T, in MITgcm is governed by the following equation in the rotated coordinates:

$$T_t = -(uT)_x - (vT)_y - (wT)_z + A_T(T_{xx} + T_{yy}) + (K_T T_z)_z. \quad (1)$$

The notations are standard, with x and y denoting the cross-basin and along-basin directions, and the continuity equation for the velocity components, $u_x + v_y + w_z = 0$, is used. The terms on the right-hand side represent the tendency terms contributed by advection, horizontal diffusion, and vertical mixing, respectively. For the time averaged temperature tendency equation, these processes can be further decomposed into mean and eddy components,

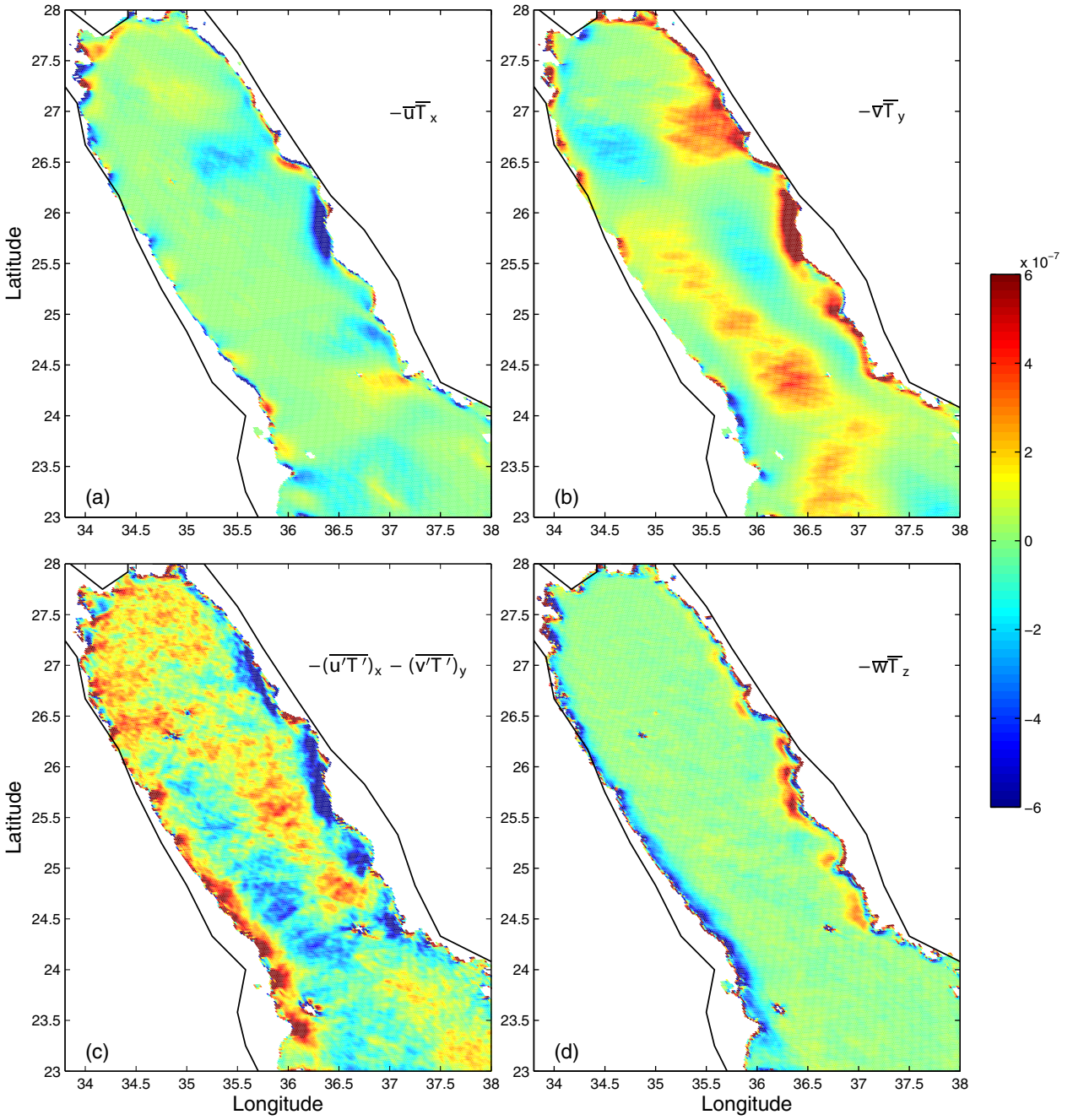

Figure 15. The mean heat balances (°C s^{-1}) at 60 m in the northern Red Sea calculated from the 50 year simulation.

$$\bar{T}_t=-\bar{u}\bar{T}_x-v\bar{T}_y-\bar{w}\bar{T}_z-(\overline{u'T'})_x-(\overline{v'T'})_y-(\overline{w'T'})_z+A_T(\bar{T}_{xx}+\bar{T}_{yy})+(K_T\bar{T}_z)_z, \quad (2)$$

where the bar denotes the time averaged component and the prime denotes the eddy component. The horizontal distributions at 60 m diagnosed from the 50 years of simulation are presented in Figure 15 for the prominent terms, including the advection by the mean horizontal velocities, the divergence of the horizontal eddy fluxes, and the advection by the mean vertical velocity. The other terms are significantly smaller near the eastern boundary and thus are not shown.

The spatial structure between the term $-\bar{u}\bar{T}_x$ (Figure 15a) and $-\bar{v}\bar{T}_y$ (Figure 15b) indicates a counteracting effect between these two terms: while the along-basin eastern boundary current supplies relatively warm

water to the boundary, which tends to increase the temperature, the eastward cross-basin current associated with the colder water in the interior of the basin tends to decrease the temperature along the eastern boundary. The eddy fluxes $[-(\overline{u'T'})_x-(\overline{v'T'})_y$ in Figure 15c] along the eastern boundary clearly play an essential role in cooling the relatively warm sinking water and tend to balance the warming associated with the downwelling ($-\bar{w}\bar{T}_z$ in Figure 15d) as suggested by the somewhat similar spatial patterns of these two terms along the boundaries. Since the isotherms are tilted along the boundary as shown in Figure 9, diapycnal mixing near the boundary is greatly enhanced by the horizontal eddy fluxes. This balance of buoyancy transports between the mean vertical advection and horizontal eddy flux close to the eastern boundary is in accordance with the results in *Cessi and Wolfe* [2009]. Furthermore, *Pedlosky and Spall* [2005] indicated that it is necessary to include the effective lateral diffusion of buoyancy near the boundary by resolved eddies or equivalent eddy diffusivity in their model to produce the intensified vertical motion near the boundary.

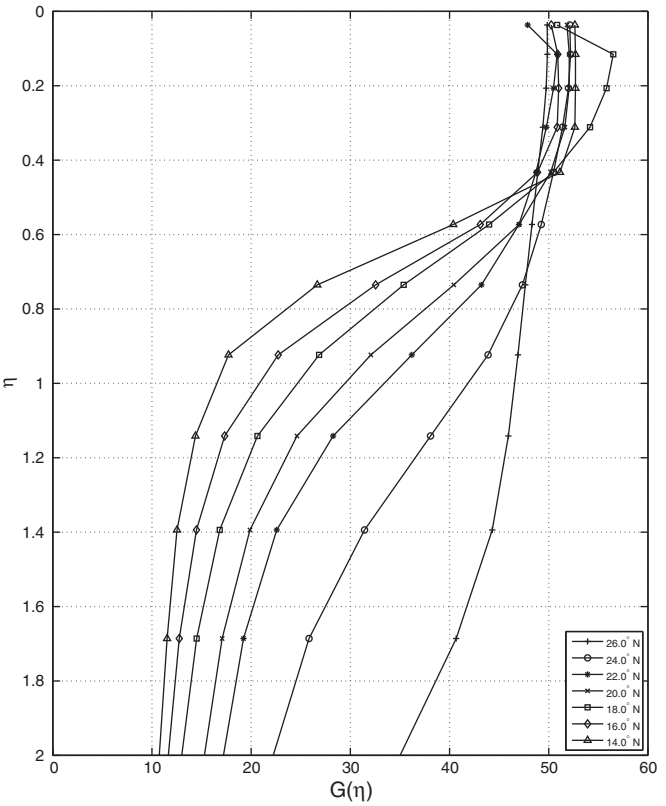

Figure 16. Scaled buoyancy profiles in February 1980, using $h = 160$ m and $B_0 = 2.0 \times 10^{-8}$ m^2 s^{-3}.

3. The Dynamics of the Overturning Circulation in the Red Sea

In this section, the dynamics that drive the complex circulation structure described above are compared with the analytical studies by *Phillips* [1966], *McCreary et al*. [1986], and *Pedlosky and Spall* [2005].

3.1. The Two-Dimensional Overturning Model

In the *Phillips* [1966] two-dimensional model, the overturning cell is limited to the depths above the sill, and a similarity solution of the buoyancy, $b = -g\,(\rho - \rho_0)/\rho_0$, is predicted by the model as

$$b=(B_0 l)^{2/3}h^{-1}G(\eta), \tag{3}$$

where B_0 is the uniform buoyancy loss at the surface, l is the distance southward from the north wall of the domain, here the northern boundary of the Red Sea, h is the sill depth, $\eta = z/h$, and $G(\eta)$ is a universal function that must generally be determined numerically. *Tragou and Garrett* [1997] analyzed hydrographic data collected in the Red Sea and found the measured $bh(B_0 l)^{-2/3}$ collapse moderately well about a universal profile when plotted together as a function of η. However, the value of the viscosity for the returning deep outflow required to produce observed overturning fluxes is unrealistically high.

Inspection of Figure 4 readily shows that the numerical solution, even when width averaged, cannot be completely self-similar. A grid of profiles of $bh(B_0 l)^{-2/3}$ for February 1980 in the model is plotted as a function of η in Figure 16. The scaled profiles for the upper layer with $\eta < 0.5$ agree reasonably well (with the exception of one), suggesting that the surface buoyancy distribution follows the $-2/3$ power rule. However, for the deep layer, the profiles are divergent. As shown in Figure 4, the temperature and salinity in the lower

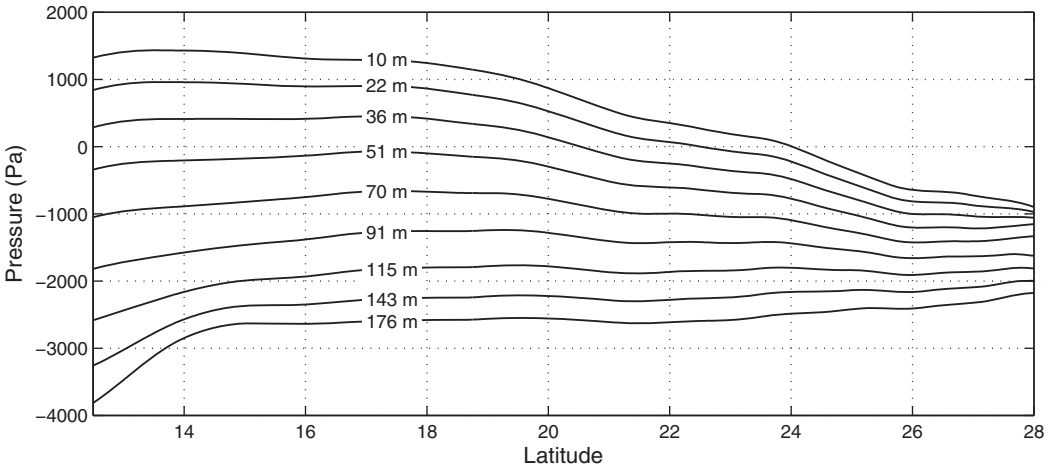

Figure 17. Perturbation pressure at different depths along the axis in the Red Sea for February 1980. Fluctuations due to eddies are removed by smoothing.

layer are almost uniform rather than stratified as calculated by *Tragou and Garret* [1997]. Finally, the dependence of the similarity solution on $\eta = z/h$ cannot capture the northward deepening of the overturning cell in Figure 4. In the model result, most of the water formed in the northern basin at depths deeper than the sill depth is exported through the strait.

Therefore, the modeled overturning circulation implies dynamical processes that are different from the similarity solution in *Phillips* [1966] model. Here the dynamics along the axis of the Red Sea are diagnosed from the model results to illustrate the two-dimensional dynamical balance. The perturbation pressures, defined as departures from a reference hydrostatic pressure profile, are plotted in Figure 17 along the axis for February 1980. The pressures are smoothed to remove the undulations caused by eddies and only the relative values at the same depth are dynamically relevant. The pressures for the upper layers, up to 91 m, show

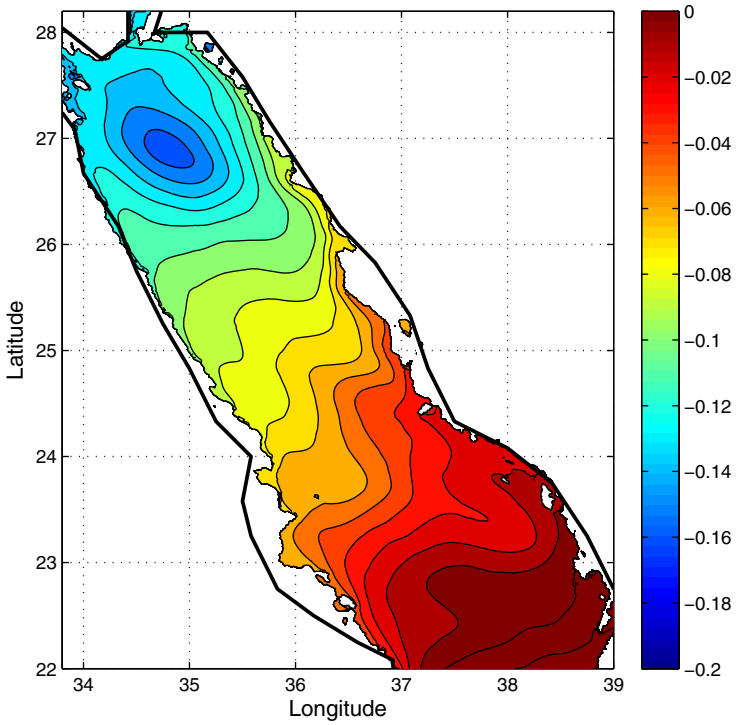

Figure 18. Sea surface height (m) in February for the climatological mean.

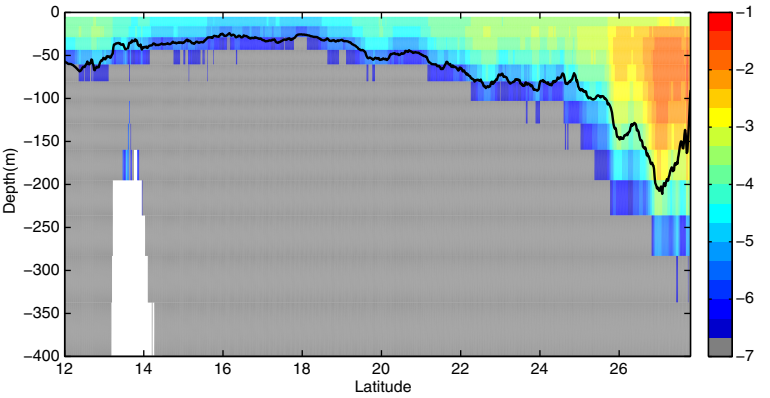

Figure 19. Axial section of logarithmic vertical viscosity ($m^2\ s^{-1}$) for February 1980. The mixed layer depths along the axis are also plotted.

northward pressure drop that increases toward the surface. This pressure gradient is related to the surface slope that is generally downward toward the north, which is caused by the decreasing temperature toward the northern Red Sea in the upper layer (Figure 18). For levels occupied by the outflow, roughly between 91 and 176 m, the pressure gradient is quite flat and the reverse pressure gradient in most parts of the basin is very weak for the outflow. However, between the strait and the Gulf of Aden south of 14°N, the pressure gradient increases markedly.

Tragou and Garret [1997] suggested that the vertical structure of the vertical eddy viscosity is an important factor in determining the two-dimensional overturning circulation. Similar to the pressure structure in Figure 17, the vertical viscosity averaged across the basin as a function of latitudes for February 1980 also shows two distinct domains for the upper and lower layers that are separated roughly by the mixed layer depths (Figure 19). The mixed layer (computed as the depth where the temperature is 0.2°C lower than the surface temperature) south of 24°N remains very shallow, less than 50 m, and it increases rapidly to over 200 m north of 24°N. While the vertical viscosity in the mixed layer is large, the vertical viscosity for the lower layer is less than $10^{-6}\ m^2\ s^{-1}$, which is much smaller than the required value of about $4 \times 10^{-2}\ m^2\ s^{-1}$ in *Phillips* [1966] similarity solution.

As in *Yao et al.* [2014], the along-basin momentum equation in a coordinate rotated along the axis of the Red Sea,

$$v_t = -p_y/\rho - fu - (uv_x + vv_y + wv_z) + (A_h v_{xx} + A_h v_{yy}) + (A_z v_z)_z, \tag{4}$$

is used here to diagnose the dynamical balance. The pressure gradient force, Coriolis acceleration, and advection terms in (4) can be directly computed from the model results. The surface wind stress is included in the vertical viscosity term, and the sum of the horizontally integrated lateral friction and the explicit bottom drag is referred to as the boundary friction term. The vertical profiles of the terms in the momentum budget for the along-basin velocity averaged for 24–28°N for February 1980 are shown in Figure 20. This is the region where the net sinking and the overturning circulation take place. The vertical profiles in the upper layer indicate an overall geostrophic balance consistent with the eastward cross-basin flow shown in Figure 10b. The Coriolis force associated with the cross-basin currents and the along-basin pressure gradient are dominant, and the latter changes direction as the cross-basin currents switch from eastward to westward at about 130 m. In the upper 60 m, the ageostrophic pressure gradient and the viscous stress due to the wind are also important. Consistent with the axial section of the perturbation pressure and vertical viscosity, all the dynamical terms for the lower layer are very weak. For regions south of 24°N (not shown here), the mean cross-basin currents are relatively weak and the along-basin pressure gradient in the upper layer is predominantly balanced by the surface wind stress.

3.2. Interpretation in Terms of Previous Three-Dimensional Models

One may appeal to previous three-dimensional models of buoyancy-driven flow with a variable Coriolis parameter, *f*, and eastern and western boundaries in an attempt to explain the three-dimensional

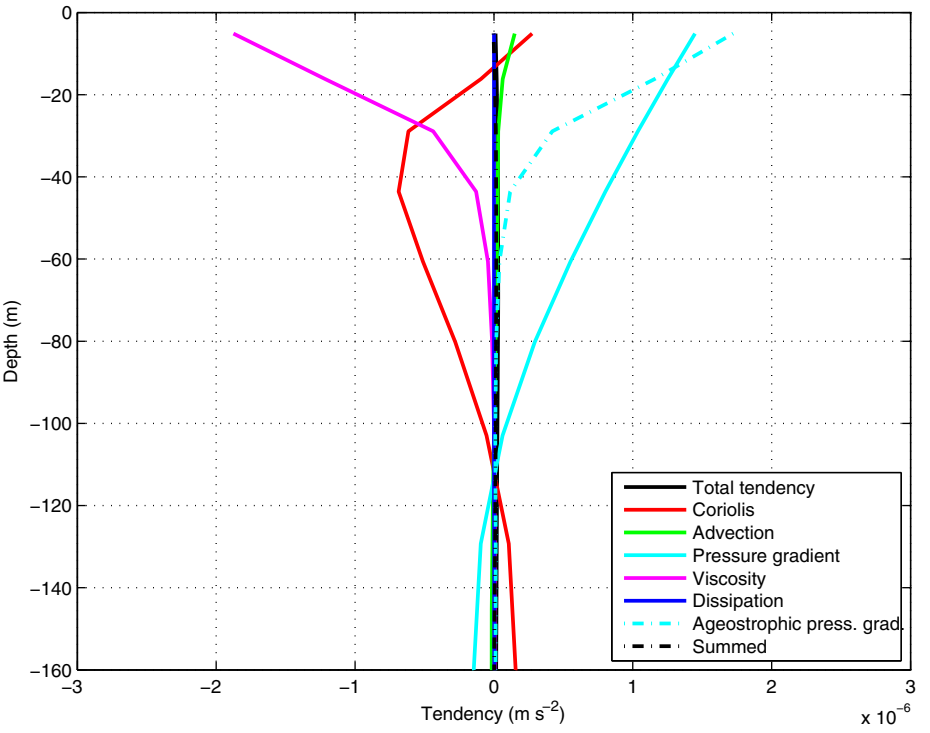

Figure 20. Along-basin momentum balance diagnosed from the model for February 1980 between 24 and 28°N.

circulation observed in our model. Notable features of our climatological winter mean include the switch from a western boundary current regime in the south to a regime with eastern and western boundary currents in the north. At the transition latitude, approximately 24°N, there is an eastward crossing flow that diverts much of the western boundary current to the eastern boundary. In addition, the major region of sinking in the climatological mean is along the eastern boundary north of 24°N. Weaker upwelling takes place along the western boundary in the north. Underlying the northward western boundary current is a countercurrent along most of the length of the Red Sea. Another feature worth noting is the northward deepening of the overturning cell, to the point where the intermediate water in the north lies well below the sill depth.

Two models of relevance are *McCreary et al.* [1986] and *Pedlosky and Spall* [2005], hereafter referred to as MSK and PS, respectively. MSK considered a linear, continuously stratified ocean, with an eastern boundary but unbounded domain to the west. The circulation is driven by wind and by an imposed density distribution at the sea surface. Their sea-surface density increases to the north, which, in combination with the thermal wind relation and a lack of motion at a greater depth, implies an eastward surface flow. This zonal flow is consistent with a northward decrease in surface pressure, as observed in our model. In addition to steady flow, MSK also allows for time-periodic motion at frequency σ associated with various baroclinic modes. PS considered a steady, two-layer ocean in a closed basin that permits only weak inflow and outflow through the boundaries. The model is forced by restoring of the density interface to a level that increases with latitude and is meant to mimic the effect of surface cooling in the north and heating in the south. The vertical velocity at the interface is parameterized by two processes, i.e., the vertical mixing and lateral diffusion of buoyancy. As in the MSK model, this implies an eastward surface flow. Both models allow for the beta effect.

A feature of both the steady MSK and the appropriately configured PS models is the eastward interior surface flow and the formation of a thermal eastern boundary layer with downwelling. This picture fits some of the characteristics of our climatological northern circulation, where eastward interior flow, an eastern boundary current, and downwelling are observed.

The time-periodic modes of the MSK model were cited by *Sofianos and Johns* [2003] in an attempt to explain the crossover latitude observed in their model solution for the mean winter circulation. They

focused on the second baroclinic mode with a frequency of $\sigma = 2\pi/(1\ \text{year})$, reasoning that variability in the Red Sea is dominated by the annual cycle, and that the vertical structure is dominated by three layers: a surface, an intermediate, and an inactive deep layer. The MSK solution for this (and all other) time-dependent modes is dependent on the latitude and sensitive to the character of the free waves that can exist at each latitude. For a given frequency, free waves are Rossby-like below, and Kelvin-like above, a critical latitude given by

$$\theta_c = \tan^{-1}(c_n/R\sigma), \tag{5}$$

where c_n is the gravity speed of vertical mode n and R is the Earth's radius. To the south of θ_c, freely propagating Rossby waves are expected to establish a western boundary layer, though the MSK model has no western boundary. To the north, the Kelvin physics establish an eastern boundary layer. The *Sofianos and Johns* [2003] estimate of θ_c is close to the 16°N transition latitude observed in their model.

This view that the crossover latitude is also the critical latitude of a seasonal oscillation is contradicted by our Red Sea model. An additional experiment, forced with *steady* atmospheric forcing retrieved from the monthly surface fluxes in February 1980, is run for 10 years starting from the state in February in 1980. Equation (5) would predict that for steady forcing, $\sigma \to 0$, θ_c approaches $\pi/2$ (the North Pole), and no crossover flow should occur in this experiment. However, the model result (not shown here) in this experiment yields a crossover latitude of 24.5°N for the surface circulation, very close to the result in the climatological mean for February with the NCEP forcing (Figure 6a).

Here we propose that the strong vertical mixing in the north (Figure 19) is a critical dynamical condition for the structure of the overturning circulation and the crossing of the western boundary current can be explained with the MKS and PS models. As shown in MKS, when the vertical mixing is reduced, the eastern boundary current tends to be weakened because it is radiated westward by Rossby waves. In contrast, strong vertical mixing damps the Rossby waves before they propagate far away from the eastern boundary. This is consistent with the strong western boundary current in the south where the vertical mixing is significantly weaker. In the PS model, for a moderate damping parameter that represents vertical mixing, the solution to the planetary geostrophic equations forced by a baroclinic exchange at the southwest corner yields a remarkably similar circulation pattern to that in the northern Red Sea in our model, including a zonal crossover flow that supplies the eastern boundary current and a cyclonic recirculation further north (see the result in their Figure 10). PS suggests that the interaction between the western boundary inflow and the recirculation creates a stagnation point along the western boundary where the crossover of the boundary currents takes place. Also in the MKS model with constant forcing, an intensified zonal flow occurs along the southern boundary of the domain and is diverted into an eastern boundary current in the north. These features are directly comparable to our model results in the Red Sea north of 24°N showing the eastward crossing flow and the eastern boundary current. Therefore, the shifting of the boundary current around 24°N appears to be a response to the change of the vertical mixing and the resulting change of dynamical balance, rather than determined by the critical latitude related to Rossby waves.

The sinking process along the boundary involves complex dynamical processes on various spatial scales. A nonzero pressure gradient along the wall, hence geostrophic currents normal to the wall, is essential for the downwelling/upwelling to occur near the wall. For the Red Sea, a general northward surface pressure drop is produced by the northward increasing density and there is a nonzero northward pressure gradient near the boundary (i.e., along the edge of the boundary layer) as indicated by the intersections of the sea surface height contours with the boundaries (Figure 18), a feature also predicted by the planetary quasi-geostrophic version of the PS model. In the northern Red Sea, surface eastward flows are present near both boundaries in response to the northward pressure gradient force (Figures 10a and 10b), leading to downwelling along the eastern boundary and upwelling along the western boundary. Furthermore, the closer contours of the sea surface height in Figure 18 indicate that the pressure gradient near the eastern boundary is larger, resulting in a stronger cross-basin current and hence stronger downwelling near the eastern boundary. The greater pressure gradient along the eastern boundary is apparently associated with the eastern boundary current, which is approximately in geostrophic balance in the direction normal to the boundary, causing the northward bending of the contours of the surface height (pressure gradient) and a stronger pressure gradient along the eastern boundary.

The PS model has a more complex distribution of upwelling and downwelling, with downwelling in the interior of the basin, upwelling in a thermal western boundary current, and downwelling in thinner "hydrostatic" layers lying very close to the western and eastern boundaries. However, the major difference between the PS model and our model is that the sinking in the PS model occurs mainly in the hydrostatic layer along the western boundary, rather than the eastern boundary. One possible explanation for the difference lies in the parameter space related to the vertical mixing. In PS, the thermal boundary layer scale σ_T is comparable to the basin width, resulting in relatively weak vertical mixing and weak damping of the Rossby waves. The result is an intensified western boundary current and intensified sinking along the western boundary. In our model, the vertical mixing is strong enough to damp the westward propagation of the Rossby waves, and there is an intensified eastern boundary current in the northern Red Sea. According to the PS model, this would lead to intensified downwelling in the hydrostatic layer along the eastern boundary. In fact, our models are more in agreement in this aspect with the MSK model in which the downwelling occurs along the eastern boundary. The idealizations present in PS, including vertical walls, the parameterization of the cross-interface velocity, and the specific ordering of parameters, together with the irregular coastal topography in our model make direct comparison of the fine structure of vertical velocities in the boundary layers and the scale parameters between the two models difficult.

3.3. Effects of the Surface Wind Stress

The surface wind stress can affect the winter overturning circulation in different ways, some of which involve complicated processes, such as the effect of enhanced vertical mixing by the surface wind stress. But there are two obvious and presumably most important ways. First, the southeasterly surface wind stress can act directly on the surface inflow, increasing the inflow in the southern Red Sea. Second, the northwesterly surface wind stress in the northern Red Sea can induce upwelling along the eastern boundary and downwelling along the western boundary due to Ekman transport. With a surface wind stress of about 0.1 Pa [see Figure 2, *Yao et al.*, 2014], the vertical velocity due to coastal upwelling close to the eastern coast is roughly estimated to be $\sim 1.0 \times 10^{-4}$ m s^{-1}, using $f = 0.5 \times 10^{-4}$ s^{-1} and a deformation radius of 20 km. The wind-driven coastal upwelling therefore has a rate comparable with the downwelling rate associated with the overturning circulation (Figure 10) and opposes the buoyancy-induced upwelling and downwelling along the boundaries. However, the wind and buoyancy-driven circulation can interact in nonlinear and complex ways, e.g., the anticyclonic wind-driven gyre in the northern Red Sea shown by *Sofianos and Johns* [2003].

The effect of the surface wind stress on the winter overturning circulation in the Red Sea is examined by an 2 year (1979–1980) experiment forced only with buoyancy fluxes as discussed in *Yao et al.* [2014]. The winter overturning circulation without surface wind stress (not shown here) shows a very similar overall pattern to that with full forcing in Figure 4. The sensitivity of the water exchange in the strait to the surface wind stress is demonstrated in Figure 13 in *Yao et al.* [2014]. The winter exchange rate in the strait is slightly reduced without the surface wind stress. Overall, this indicates that the winter overturning is mainly driven by thermohaline forcing and the net effect of the surface wind stress is to increase the overturning circulation slightly and this conclusion agrees with the finding by *Sofianos and Johns* [2003].

The opposing wind-driven upwelling and downwelling along the coasts, although comparable to those driven by buoyancy, appear to have a negligible effect on the overturning circulation. A simple explanation is that there would be no net sinking associated with the wind-driven downwelling and upwelling averaged across the basin. However, due to the nonlinear interaction between the wind-driven and buoyancy-driven circulation and the presence of energetic mesoscale eddies, numerical experiments run with separate wind-forcing and buoyancy forcing for multiple decades are necessary to show the effect of winds on the overturning circulation.

4. Dynamics in the Strait

Straits often provide mechanisms that limit the exchange or that block information carried in internal waves from entering the marginal sea from the open ocean. As discussed in *Yao et al.* [2014], hydraulic control could block internal waves from entering the Red Sea, hence limiting the water exchange between the Red Sea and the Gulf of Aden. In the absence of hydraulic control, friction from the lateral or bottom boundaries of the strait, or at the interface between the inflow and outflow, will generally balance the subsurface

pressure gradient between the Gulf of Aden and the Red Sea. While the summer exchange does not suggest the existence of a control point, with an increased exchange rate in winter, the exchange flow for the winter overturning circulation may become hydraulically controlled.

The hydraulics in the strait is examined with the formula for the generalized two-layer composite Froude number given in *Yao et al.* [2014]. The layer interface is defined by the inflow/outflow structure in the strait, varying across the basin, and the averaged densities for the inflow and the outflow are taken as the layer densities. The structure of the water exchange along the strait and composite Froude numbers are presented in Figure 21. The surface inflow and deep outflow are separated by the thermocline and halocline located at about 90 m in the strait. The maximum outflow occurs at similar locations around the Hanish Sill and Perim Narrow as in summer, but with larger values at deeper depths of about 120 m. Even though there is a hint of spilling of the outflow southward across the Hanish Sill (around 13.6°N), the two-layer composite Froude numbers suggest that the exchange flow is subcritical everywhere along the strait. This means that for the winter condition, the exchange flow in the strait is not hydraulically controlled. Moderate hydraulic effects are observed in terms of spilling over topographic features, but hydraulic control according to conventional two-layer measures is not found. This is in agreement with an analysis by *Pratt et al*. [2000] of wave modes based on data collected at the Hanish Sill and Perim Narrows. A caveat in the above results as discussed in *Yao et al.* [2014] is that the model has deeper depth of 160 m at the Hanish Sill than the 137 m reported by *Lambeck et al*. [2011]. A crude estimate of the composite number with reduced depth at the sill is carried out, and the Froude number is slightly increased but remains less than one, suggesting a subcritical exchange flow with reduced depth at the sill.

To explore other dynamical mechanisms that might limit the exchange in the strait, the along-strait momentum balance for February 1980 is diagnosed directly from the model and the averaged profiles of dynamical terms for the along-strait velocity are shown in Figure 22. In the upper 60 m, the main balance is between the surface wind stress (contained in the term labeled "viscosity") and the pressure gradient (due mainly to the northward sea surface slope). In the deep outflow, the boundary friction and advective terms acts with similar importance to balance the large pressure gradient. The vertical viscosity, with the maximum effect occurring around the interface at around 100 m, is substantially smaller than the boundary friction and advective terms but not negligible. The decreasing salinity and increasing temperature in the downstream direction of the outflow is also an indication of vertical mixing across the interface. Therefore, the water exchange in the strait is limited by the bottom, lateral, and interfacial drag, and is also affected by the wind.

5. Summary and Conclusions

The winter overturning in the Red Sea is analyzed from a 50 year MITgcm simulation in this study (presented in two parts) in order to analyze its three-dimensional circulation structure and to clarify some of the underlying dynamics. It is shown in [*Yao et al.*, 2014] that the model produces a seasonal exchange structure in the strait that is in good agreement with the observations by *Sofianos et al*. [2002]. The winter overturning circulation of the MITgcm simulation exhibits complex circulation with a three-dimensional structure that is quite different from previous modeling studies by *Eshel and Naik* [1997] and *Sofianos* and *Johns* [2002; 2003].

During the winter overturning circulation, the northern Red Sea, the southern Red Sea, and the strait demonstrate different dynamics. One of the most important and intriguing findings is that the sinking in the overturning circulation takes place in a narrow boundary layer close to the eastern boundary north of 24°N. The boundary layer has a thickness of about 20 km, which is comparable with the local deformation radius. This result from our model study with realistic topography and atmospheric forcing shares a similar sinking pattern with the idealized model studies by *Spall* [2003, 2004]. It is shown from our model that, within the boundary layer, the buoyancy balance between the vertical mean advection and horizontal diffusion by eddy fluxes is a critical dynamical process for the intensified downwelling and upwelling near the boundary. Our model also suggests that the downwelling or upwelling in the boundary layer is mostly balanced by the flow normal to the boundary, which agrees with *Cessi and Wolfe* [2009].

Meanwhile, weaker upwelling in a thin layer takes place along the western boundary. The net sinking process in the northern Red Sea is accomplished through a cross-basin overturning circulation north of 24°N,

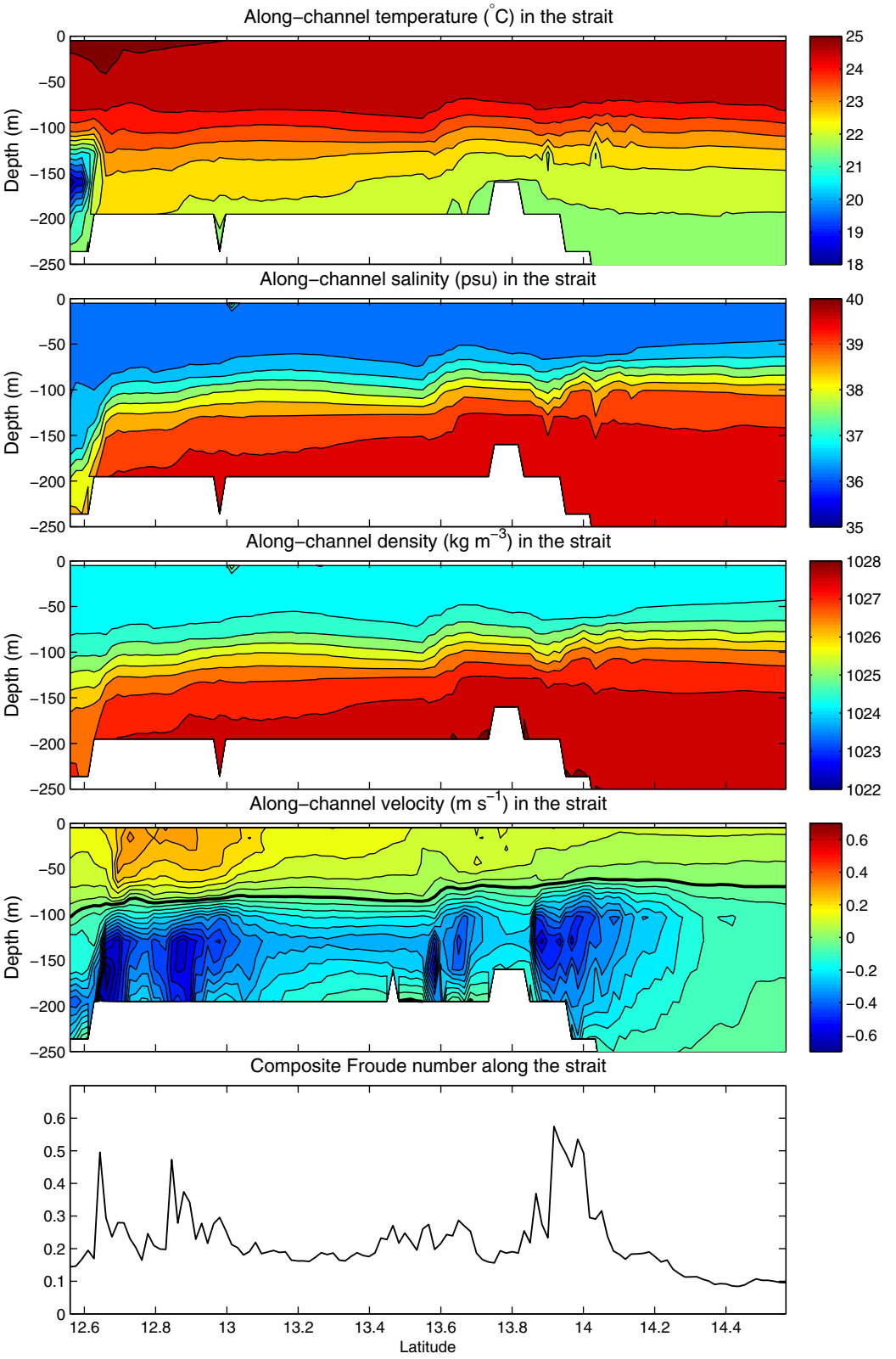

Figure 21. Salinity, temperature, vertical density, along-channel velocity average across the strait, and generalized composite Froude number along the strait for February 1980.

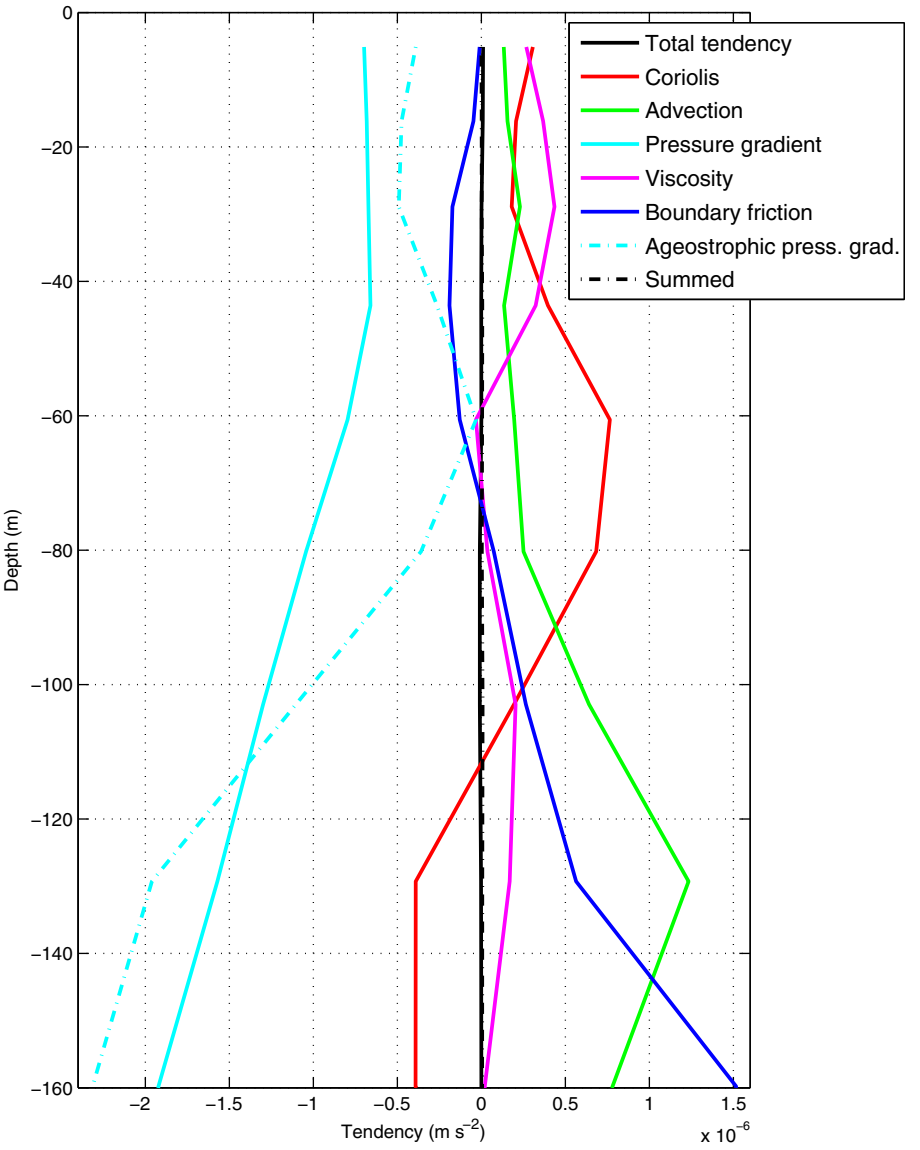

Figure 22. Along-strait momentum balance diagnosed from the model for February 1980 in the strait.

which can be decomposed into two components. The first one has an overturning rate associated with the upwelling along the western boundary but without contributing to the general along-basin overturning circulation in the Red Sea. The second one, supplied by the recirculating gyre, sinks only along the eastern boundary and constitutes the general along-basin overturning circulation in the Red Sea (Figure 14).

There are very limited observational data regarding the sinking processes, and direct observation of the vertical velocity is very challenging because of its small magnitude of $\sim 10^{-4}$ m s^{-1}. The water exchange in the strait imposes a strong constraint on the overturning circulation in the Red Sea. The volume transports in the strait in the model [Figure 3, *Yao et al.*, 2014] show almost perfect agreement with the observations by *Sofianos et al*. [2002] and the production rate of outflow water directly integrated from the vertical velocity is also in very good agreement with the estimate in the strait (Figure 11). To our knowledge, this is the first simulation of sinking along the boundaries of a realistic basin and it is a step forward in understanding buoyancy-driven circulation, not only in the Red Sea but also in other marginal seas. The sinking process along the boundary is also supported by previous idealized, analytical and experimental studies [*Spall and Pickart*, 2001; *Spall*, 2003, 2004; *Pratt and Spall*, 2008; *Pedlosky* and *Spall* 2005; *Cenedese*, 2012]. These comparisons give us confidence that the sinking process as suggested in the model is physically plausible. The

model results also give some guidance on future observational efforts targeting the sinking process to see if the model results are realistic.

The circulation in the northern Red Sea agrees to a large extent with the three-dimensional analytical models by *McCreary et al*. [1986] and *Pedlosky and Spall* [2005]. The surface pressure gradient resulting from the northward density gradient, effective vertical mixing, and horizontal diffusion are considered as integral dynamical processes in the modeled circulation structure. The surface pressure gradient in the northern Red Sea along the basin requires a cross-basin interior eastward flow, resulting in downwelling in the east and upwelling in the west. The vertical mixing damps the westward propagation of Rossby waves that form the strong western boundary current in the southern Red Sea. The crossover of the current around 24°N and the eastern boundary current farther north is a result of the increased vertical mixing and resulting dynamical balance. The horizontal diffusion by eddy flux is essential in the boundary layer for the buoyancy balance in converting the less dense sinking water into denser water. The eastern boundary current leads to a stronger pressure gradient along the outside edge of the boundary layer than in the west. Due to the stronger pressure gradient along the boundary, a stronger geostrophic cross-basin flow supplied by a cyclonic recirculating gyre induces stronger downwelling along the eastern boundary than the upwelling along the western boundary. In the basin south of 24°N, where the vertical mixing is weak, both the surface inflow and the intermediate outflow are intensified along the western boundary.

The hydraulic analysis and momentum balance analysis in the strait suggest that the limiting processes for the exchange in the strait are not a result of hydraulic control, at least not when measured with respect to a month-long mean for February 1980. We do note, however, that the sill depth in the model is slightly greater than the actual value. The lack of hydraulic control is in agreement with *Pratt et al*. [2000]. The bottom and lateral friction, and, to a lesser extent, the internal friction around the interface, balance the larger pressure gradient toward the Gulf of Aden and limit the transport of the outflow.

In the results for specific years, such as 1980, the eddies are so dominant that the horizontal structures presented in the climatological mean results are not identifiable. As shown in Figure 4, the eddies can alter the overturning structure on smaller scales. The irregular shape of the basin and the complex bathymetry used in the model complicate a detailed study of the role of the eddies in the overturning circulation. An idealized model configured with simple but essential topographic features is warranted to fully investigate the role of the eddies in the winter overturning circulation. The complex structure of the downwelling and upwelling and the dynamical balance in the boundary layer suggested by *Pedlosky and Spall* [2005] can also be further investigated in the idealized modeling study.

Acknowledgments
Partial support for this effort was provided by the Saudi Aramco Marine Environmental Research Center at KAUST. We thank three anonymous reviewers for comments and suggestions that improved the manuscript.

References

Biton, E., H. Gildor, and W. R. Peltier (2008), Red sea during the last glacial maximum: Implications for sea level reconstruction, *Paleoceanography*, *23*, PA1214, doi:10.1029/2007pa001431.
Cember, R. P. (1988), On the sources, formation, and circulation of Red Sea deep water, *J. Geophys. Res.*, *93*, 8175–8191.
Cenedese, C. (2012), Downwelling in basins subject to buoyancy loss, *J. Phys. Oceanogr.*, *42*, 1817–1833.
Cessi, P., and C. L. Wolfe (2009), Eddy-driven buoyancy gradients on eastern boundaries and their role in the thermocline, *J. Phys. Oceanogr.*, *39*, 1595–1614.
Eshel, G., and N. H. Naik (1997), Climatological coastal jet collision, intermediate water formation, and the general circulation of the Red Sea, *J. Phys. Oceanogr.*, *27*, 1233–1257.
Lambeck, K., A. Purcell, N. C. Flemming, C. Vita-Finzi, A. M. Alsharekh, and G. N. Bailey (2011), Sea level and shoreline reconstructions for the Red Sea: Isostatic and tectonic considerations and implications for hominin migration out of Africa, *Quat. Sci. Rev.*, *30*(25–26), 3542–3574, doi:10.1016/J.Quascirev.2011.08.008.
McCreary, J. P., S. R. Shetye, and P. K. Kundu (1986), Thermohaline forcing of eastern boundary currents—with application to the circulation off the west-coast of Australia, *J. Mar. Res.*, *44*, 71–92.
Murray, S. P., and W. Johns (1997), Direct observations of seasonal exchange through the Bab el Mandab Strait, *Geophys. Res. Lett.*, *24*, 2557–2560.
Pedlosky, J., and M. A. Spall (2005), Boundary intensification of vertical velocity in a beta-plane basin, *J. Phys. Oceanogr.*, *35*, 2487–2500.
Phillips, O. M. (1966), On turbulent convection currents and the circulation of the Red Sea, *Deep Sea Res., Part A*, *13*, 1149–1160.
Plahn, O., B. Baschek, T. H. Badewien, M. Walter, and M. Rhein (2002), Importance of the Gulf of Aqaba for the formation of bottom water in the Red Sea, *J. Geophys. Res.*, *107*(C8), doi:10.1029/2000jc000342.
Pratt, L. J., H. E. Deese, S. P. Murray, and W. Johns (2000), Continuous dynamical modes in straits having arbitrary cross sections, with applications to the Bab al Mandab, *J. Phys. Oceanogr.*, *30*(10), 2515−2534.
Pratt, L. J., and M. Spall (2008), Circulation and exchange in choked marginal seas, *J. Phys. Oceanogr.*, *38*(12), 2639–2661.
Sofianos, S. S., and W. E. Johns (2002), An Oceanic General Circulation Model (OGCM) investigation of the Red Sea circulation. 1. Exchange between the Red Sea and the Indian Ocean, *J. Geophys. Res.*, *107*, 3196, doi:10.1029/2001JC001185.
Sofianos, S. S., and W. E. Johns (2003) An Oceanic General Circulation Model (OGCM) investigation of the Red Sea circulation: 2. Three-dimensional circulation in the Red Sea, *J. Geophys. Res.*, *108*, 3066, doi:10.1029/2001JC001185.

Sofianos, S., W. E. Johns, and S. P. Murray (2002), Heat and freshwater budgets in the Red Sea from direct observations at Bab el Mandeb, *Deep Sea Res., Part II*, *49*, 1323–1340.

Sofianos, S. S., and W. E. Johns (2007), Observations of the summer Red Sea circulation, *J. Geophys. Res.*, *112*(C6), C06025, doi:10.1029/2006jc003886.

Spall, M. A. (2003), On the thermohaline circulation in flat bottom marginal seas, *J. Mar. Res.*, *61*, 1–25.

Spall, M. A. (2004), Boundary currents and watermass transformation in marginal seas, *J. Phys. Oceanogr.*, *34*, 1197–1213.

Spall, M. A., and R. S. Pickart (2001), Where does dense water sink? A subpolar gyre example, *J. Phys. Oceanogr.*, *31*, 810–826.

Tragou, E., and C. Garrett (1997), The shallow thermohaline circulation of the Red Sea, *Deep Sea Res., Part I*, *44*, 1355–1376.

Woelk, S., and D. Quadfasel (1996), Renewal of deep water in the Red Sea during 1982–1987, *J. Geophys. Res.*, *101*, 18,155–18,165.

Wyrtki, K. (1974), On the deep circulation of the Red Sea, in *L'oceanographie physique de la Mer Rouge*, pp. 135–163, Cent. Natl. pour l'Exploitation des Oceans, Paris.

Yao, F., I. Hoteit, L. J. Pratt, A. S. Bower, P. Zhai, A. Köhl, G. Gopalakrishnan (2014), Seasonal overturning circulation in the Red Sea: 1. Model validation and summer circulation, *J. Geophys. Res. Oceans*, *119*, doi:10.1002/2013JC009004.